Geochemical and geochronological constraints on the Mesoproterozoic Red Granite Suite, Kunene AMCG Complex of Angola and Namibia

Lorenzo Milani[a,*], Jérémie Lehmann[b], Grant M. Bybee[c], Ben Hayes[c], Trishya M. Owen-Smith[b], Lize Oosthuizen[a], Pieter W.J. Delport[a], Henriette Ueckermann[b]

[a] Department of Geology, University of Pretoria, Private Bag X20, Hatfield 0028, South Africa
[b] Department of Geology, University of Johannesburg, P.O. Box 524, Auckland Park 2006, Johannesburg, South Africa
[c] School of Geosciences, University of the Witwatersrand, 1 Jan Smuts Avenue, Braamfontein 2000, Johannesburg, South Africa

*Corresponding author. Email: lorenzo.milani@up.ac.za

Highlights

- A-type granitoids not only related to extensional environments;
- Time-space relation between anothosite and MCG (mangerite-charnockite-granite) components;
- Tectonic setting of AMCG complexes compatible with contractional tectonics.

Abstract

Anorthosite-mangerite-charnockite-granite (AMCG) suites form large batholiths emplaced during the Proterozoic Eon. Magma source(s), emplacement mechanisms, and the tectonic setting of AMCG suites remain poorly understood. We present new major and trace element geochemistry combined with U-Pb zircon geochronology and Lu-Hf isotopes for the Red Granite Suite, part of the Mesoproterozoic Kunene AMCG Complex (Angola and Namibia), and its Paleoproterozoic host rocks, to elucidate the petrogenesis and tectonic setting of the Kunene Complex granitoids. The studied samples are mostly granite with minor syenite and quartz monzonite. LA-MC-ICPMS U-Pb zircon dates indicate that felsic magmatism was active for at least 90 Myr (1450–1360 Ma) and shows spatial and temporal similarities with emplacement of the main anorthositic body. The geochemistry of the granitoids did not change substantially over time, with predominant alkali-calcic, A-type granites. The $\varepsilon Hf_{(t)}$ of zircon grains in the Red Granite Suite ranges between −11.3 and + 1.6. These results, when considered together with Hf isotopic compositions of zircon from the Paleoproterozoic host rocks ($\varepsilon Hf_{(t)}$ = -11.3 to + 0.4) and xenocrysts in the Red Granite, suggest the suite is derived from the mixing of a Paleoproterozoic crustal component with juvenile mantle-derived material. Syn-magmatic east–west shortening has been documented in both the anorthosites and Red Granites at the southwestern margin of the Kunene Complex in the period 1400–1380 Ma. The results from the Hf isotopes on zircon, combined with the long-lived nature of magmatism, the *syn*-contractional magmatism, at least locally, and the requirement for extensive crustal melting, suggest that the Red Granite Suite was formed in a convergent margin setting. This challenges the traditional view that A-type granitoids are restricted to anorogenic, extensional settings, and is in agreement with recent views on the petrogenesis of massif-type anorthosites and their associated MCG magmatism.

Keywords: Kunene; AMCG suites; Granites; U-Pb geochronology; Lu-Hf isotope system

1. Introduction

Large volumes of intermediate to felsic rocks, including granitoids, mangerite and charnockite, are typically associated with massif-type anorthosites, which are intrusive rocks dominated by modal plagioclase (Ashwal, 1993). These associations are collectively known as AMCG (anorthosite-mangerite-charnockite-granite) suites (Emslie, 1978, Emslie et al., 1994, McLelland et al., 2004), and have been documented worldwide (e.g., Chatterjee et al., 2008a, Chatterjee et al., 2008b, McLelland et al., 2010, and references therein; Shumlyanskyy et al., 2017, Wang et al., 2020, and references therein). AMCG suites, mainly Proterozoic in age, still present unresolved dilemmas with regards to magma source(s) and tectonic setting, and multiple models have been proposed to explain their emplacement mechanisms (Emslie, 1978, Morse, 1982, Wiebe, 1992, Ashwal, 1993; McLelland et al., 1996, 2010; Myers et al., 2008, Bybee et al., 2014, Ashwal and Bybee, 2017, Slagstad et al., 2018, Lehmann et al., 2020, and references therein). The granitoids of AMCG suites can exceed the volume of the anorthosites (McLelland et al., 2010). Early studies suggested that AMCG suites formed from a fractionated crustal melt that was intermediate in composition (Michot, 1960, de Waard, 1968). More recently, however, evidence has been provided indicating that MCG rocks are coeval, but not comagmatic, with the anorthositic and mafic components of AMCG suites (McLelland et al., 2010). Melting of the lower crust due to ponding of primitive magmas at the crust-mantle interface is invoked as a trigger to produce a large proportion of MCG rocks (Emslie, 1975, Emslie, 1978, Emslie et al., 1994, McLelland et al., 2010).

The tectonic setting of AMCG suites is still unclear. The apparent absence of *syn*-contraction tectonic fabrics in AMCG rocks has been used to support an extensional setting for these suites (e.g., Emslie, 1978), but an overall contractional environment accompanied by late-stage orogenic extension has also been proposed (Corrigan and Hanmer, 1997). On the basis of tectonic, petrographic, and geochronological evidence, reactivation of lithospheric sutures and involvement of processes like slab break-off, back-arc extension, and post-orogenic collapse during lithosphere delamination have also been invoked in the petrogenesis of AMCG suites (Corrigan and Hanmer, 1997, Scoates and Chamberlain, 1997, Myers et al., 2008, McLelland et al., 2010, Wang et al., 2020). Further insights are required from AMCG suites in order to determine their tectonic setting.

Granites in AMCG suites show a typical A-type character, being dominantly potassic and rich in alkalis (K_2O + Na_2O), high field-strength elements (HFSE), FeO_{tot}/MgO and Ga/Al (e.g., Whalen et al., 1987, Eby, 1992, Frost and Frost, 2011). Traditionally, A-type granites have been assigned to a variety of extensional regimes, such as back-arc basins, post-collisional settings, or within-plate settings (Pearce et al., 1984, Whalen et al., 1987, Pearce, 1996). However, other authors have challenged this view, showing that A-type granites can also be emplaced during crustal contraction (Ren et al., 2021, and references therein). Similarly, AMCG suites can form during crustal shortening related to arc accretion, basin closure and collision, with examples such as the gabbro-anorthosite rocks in the Eastern Ghats Mobile Belt, India (e.g., Dobmeier, 2006, Nagaraju et al., 2008) and the composite gabbro-mangerite-charnockite-granite intrusions of the Lofoten–Vesterålen suite, Norway (Corfu, 2004).

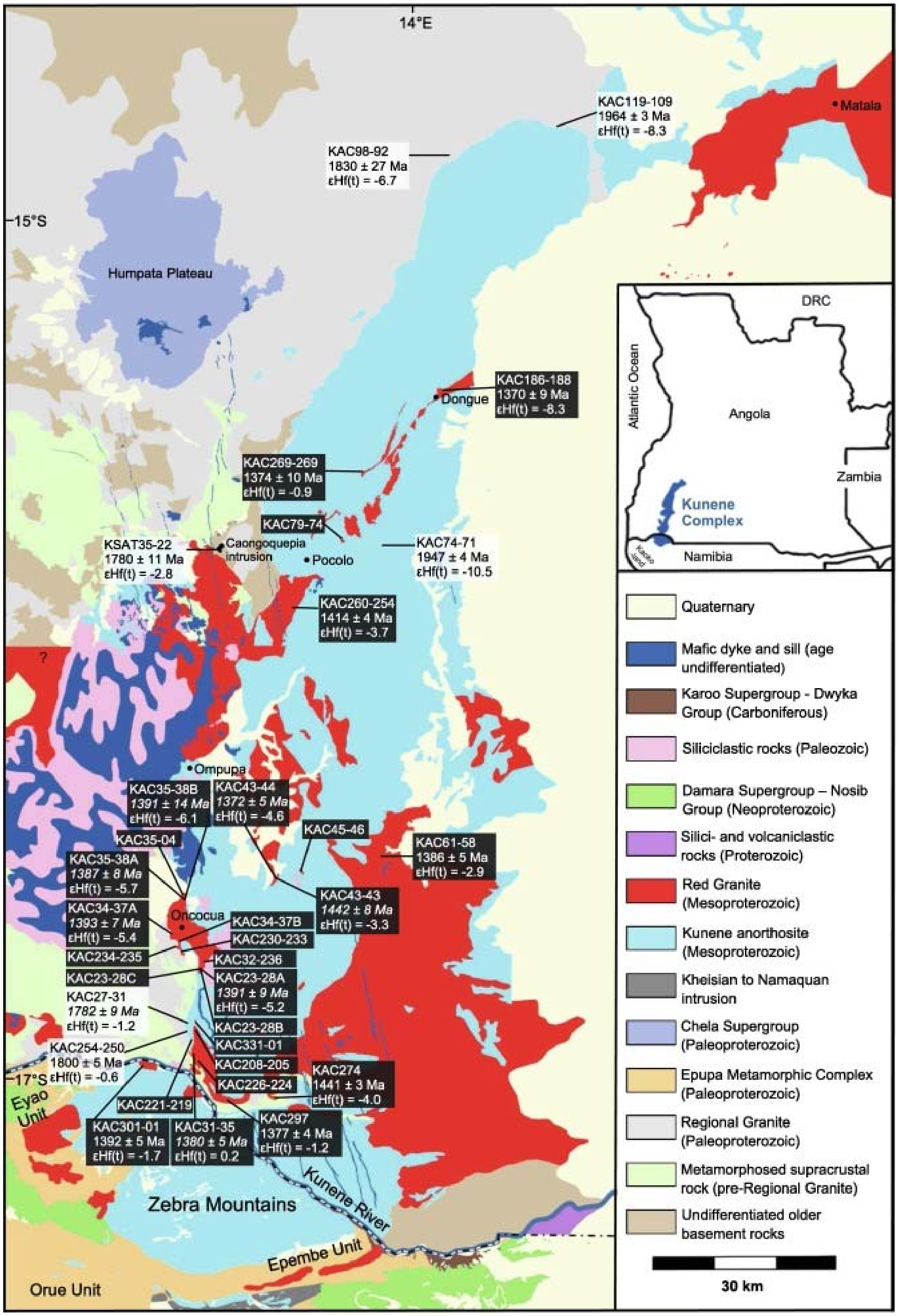

Fig. 1. Geological map of the Kunene Complex and surrounding rocks in southwestern Angola and northern Namibia (after Serviços De Geologia E Minas De Angola 1:100 000, 1:250 000, and 1:1 000 000 maps; Geological Survey of Namibia 1:250 000 map; Seth et al., 2005, McCourt et al., 2013, Brandt et al., 2021). Boxes report U-Pb age and average $\varepsilon Hf_{(t)}$ for dated samples. Black boxes: Red Granite Suite; 21 of the 27 rocks have been analyzed for major and trace elements (Table 1). White boxes: basement host rocks. In italics: U-Pb ages published by Lehmann et al. (2020). Inset map shows the position of the Kunene AMCG Complex in southwestern Africa. Datum is WGS84 and projection is UTM zone 33 south.

Table 1. Major and trace element analytical geochemistry of representative Red Granite Suite rocks.

Rock type	Syenite	Syenite	Qz monzonite	Qz monzonite	Qz monzonite	Qz monzonite	Qz monzonite	Granite	Granite	Granite	Granite	Granite	Granite	Granite	Granite	Granite	Granite	Granite	Granite	Granite	Granite
sample	KAC 79-74	KAC 234-235	KAC32-236	KAC230-233	KAC260-254	KAC331-1	KAC34-37B	KAC 23-28B	KAC 23-28C	KAC 31-35	KAC 35-4	KAC 61-58	KAC 186-188	KAC 226-224	KAC 274	KAC 45-46	KAC 269-269	KAC 297	KAC 43-45	KAC 208-205	KAC 221-219
Long E (dec deg)	13.835466	13.476294	13.488411	13.474290	13.708975	13.461700	13.441027	13.485900	13.485900	13.469986	13.449689	13.923343	14.081797	13.476349	13.635403	13.747779	13.889764	13.538857	13.678043	13.459035	13.463068
Lat S (dec deg)	15.784389	16.763058	16.767013	16.765471	15.923305	16.869249	16.681810	16.781190	16.781190	16.941510	16.593061	16.499553	15.414246	16.937279	17.086877	16.547995	15.595566	17.075111	16.550546	16.910502	16.932399
	A-type	A-type	A-type	A-type	A-type	A-type	A-type	A-type	A-type	A-type	A-type	A-type	A-type	A-type	A-type	A-type	A-type	A-type	I-type	I-type	I-type
SiO_2	52.7	59.1	63.1	60.7	66.9	67.5	67.0	68.4	64.6	75.1	72.7	72.8	71.0	74.1	72.6	76.7	76.3	76.4	75.3	71.0	73.9
TiO_2	0.84	1.41	0.92	1.19	0.39	0.57	0.38	0.50	0.77	0.16	0.33	0.19	0.16	0.19	0.44	0.07	0.08	0.07	0.03	0.23	0.12
Al_2O_3	13.9	14.3	14.6	14.6	14.9	14.9	15.2	14.2	16.0	12.1	15.0	12.5	13.9	12.3	13.0	13.2	12.2	11.9	13.6	14.9	13.7
Fe_2O_3	1.62	0.98	0.68	0.87	0.50	0.43	0.34	0.42	0.58	0.24	0.29	0.30	0.31	0.29	0.30	0.08	0.15	0.17	0.06	0.17	0.11
FeO	10.8	6.56	4.56	5.77	3.36	2.84	2.30	2.81	3.84	1.61	1.92	2.03	2.04	1.95	1.97	0.54	0.97	1.12	0.39	1.11	0.77
MnO	0.37	0.16	0.12	0.14	0.07	0.07	0.05	0.07	0.07	0.03	0.04	0.04	0.04	0.03	0.02	0.01	0.02	0.02	0.01	0.03	0.02
MgO	0.27	1.59	1.52	1.35	0.26	0.77	0.56	0.68	1.33	0.15	0.65	0.22	0.17	0.20	0.48	0.22	0.12	0.29	0.13	0.62	0.33
CaO	6.14	2.65	2.81	3.38	1.49	1.95	1.32	1.71	3.11	0.25	0.94	0.99	1.81	0.26	0.83	1.37	0.21	0.06	0.76	1.01	1.05
Na_2O	4.87	3.81	3.60	3.29	4.00	3.37	3.24	3.20	6.36	3.26	1.94	3.18	4.07	3.10	4.73	0.70	3.70	3.99	3.53	4.16	4.42
K_2O	4.09	5.03	4.41	4.94	5.56	5.76	6.64	5.46	0.67	5.46	4.36	5.90	4.73	5.60	4.19	5.64	4.65	4.54	5.25	4.47	4.17
P_2O_5	0.28	0.76	0.42	0.59	0.10	0.22	0.16	0.19	0.33	0.04	0.14	0.04	0.04	0.06	0.10	0.00	0.00	0.00	0.00	0.10	0.02
LOI	1.00	1.12	1.47	0.83	0.69	0.46	1.06	0.87	1.22	0.72	0.81	0.63	0.74	0.81	0.41	0.93	0.90	0.71	0.50	1.08	0.72
Total	95.8	97.5	98.2	97.7	98.2	98.8	98.3	98.4	98.9	99.0	99.1	98.8	99.1	98.8	99.1	99.4	99.3	99.3	99.6	98.9	99.3
Ba	1497	2136	1536	2131	1907	1230	1899	1463	210.7	423.8	1363	1102	466.5	906.5	735.4	57.8	53.9	118.3	135.8	993.7	571.4
Co	1.21	11.2	7.19	10.1	1.52	4.46	3.00	4.39	8.24	1.61	4.29	1.46	1.65	0.48	1.82	0.96	1.85	0.39	1.20	2.69	1.54
Cr	51.7	49.1	37.1	18.6	64.5	82.0	68.3	35.2	72.5	133.4	87.6	98.9	64.2	60.9	102.6	127.5	36.0	72.6	70.3	84.7	135.4
Cs	0.04	0.15	1.34	0.23	2.58	0.62	0.36	0.26	0.18	2.28	0.64	0.46	0.10	2.65	0.45	0.64	1.97	2.25	0.10	0.62	1.01
Cu	18.3	12.8	8.01	9.96	7.82	5.59	11.7	8.53	6.30	7.84	13.8	3.00	3.99	4.50	4.75	2.69	1.85	10.8	2.12	4.41	34.0
Ga	33.1	41.3	37.9	35.6	26.7	26.5	30.4	25.1	28.6	26.8	20.4	36.9	39.7	21.5	19.6	14.7	24.5	24.9	13.7	19.5	13.1
Hf	2.13	1.37	2.57	2.00	4.49	4.33	1.58	2.62	2.89	10.3	1.61	3.15	8.58	7.91	9.21	0.77	13.24	14.76	1.79	3.39	3.29
Li	2.37	12.00	28.56	8.09	14.5	14.0	10.8	7.38	8.38	1.56	13.27	6.75	1.11	1.59	1.77	1.27	1.17	4.55	0.62	6.95	2.27
Mo	27	34	26	33	36	35	19	34	37	< d.l.	27	30	31	24	38	23	20	29	< d.l.	24	19
Nb	60.7	53.8	38.8	51.0	29.6	37.9	30.8	27.7	28.9	38.4	20.4	18.8	41.8	31.5	24.4	63.6	55.6	62.0	0.70	3.92	5.58
Ni	1.34	2.40	2.90	2.48	1.92	3.52	2.16	3.90	4.69	4.49	3.83	3.63	1.92	1.65	3.00	2.84	1.85	1.69	2.14	4.62	3.38
Pb	14.3	27.9	26.3	27.1	23.8	32.6	27.1	27.9	9.43	25.3	26.3	21.3	6.96	22.8	8.46	4.56	21.1	29.0	21.6	23.5	15.8
Rb	46.6	88.0	102.4	82.2	142.2	140.2	122.7	102.7	14.4	196.3	130.7	96.1	61.7	177.6	93.1	21.7	191.3	254.3	75.2	92.6	84.4
Sc	9.08	18.9	12.5	18.4	6.56	7.26	7.49	6.72	7.99	1.45	8.08	2.50	3.44	3.17	5.53	0.99	0.20	0.78	0.31	2.86	2.05
Sn	0.42	3.49	5.93	3.55	6.40	4.10	3.06	1.51	3.88	14.4	2.97	8.16	7.51	10.5	10.3	4.90	11.7	24.6	0.34	4.30	3.68
Sr	120.3	308.7	321.3	291.8	153.3	244.1	278.4	236.3	317.2	20.3	246.8	91.3	353.5	31.9	93.4	287.9	7.27	4.21	29.0	416.2	245.3

Ta	1.75	1.80	1.53	1.71	1.56	1.47	1.00	0.87	0.99	2.53	0.86	0.78	2.17	2.01	1.56	1.53	2.77	3.63	0.04	0.15	0.51
Th	0.61	6.04	12.4	3.83	12.4	10.1	8.94	2.50	8.32	22.23	4.93	28.4	16.3	21.4	23.0	15.7	23.5	42.0	0.48	14.5	10.2
U	0.20	0.27	1.59	0.39	3.45	1.54	0.56	0.46	0.73	6.67	0.97	1.19	2.74	6.33	5.66	2.75	4.90	6.10	0.33	1.62	2.43
V	4.57	44.7	38.6	41.1	9.09	30.2	15.4	24.0	42.8	12.6	30.6	10.5	16.0	5.18	24.6	11.0	2.96	11.4	6.19	21.8	18.2
W	0.56	0.34	0.41	0.32	0.98	0.53	0.37	0.25	0.41	1.58	0.45	0.51	0.54	1.15	1.42	0.55	0.68	0.85	0.29	0.41	0.50
Y	67.0	77.1	60.1	75.5	44.2	44.0	44.8	41.6	44.8	71.4	33.3	36.9	58.6	41.1	43.7	27.0	38.9	87.5	0.94	2.62	5.97
Zn	335.1	174.6	119.2	158.9	116.5	70.8	62.0	71.2	58.4	75.2	61.4	56.2	13.2	55.2	16.5	14.2	46.0	29.3	8.96	37.5	13.3
Zr	90.6	41.5	78.0	63.0	152.6	154.2	51.4	89.5	101.2	267.6	50.6	96.6	235.0	232.4	308.0	12.6	314.6	283.3	37.4	124.9	100.0
La	50.0	191.5	161.7	117.4	58.2	83.0	129.7	68.8	103.2	56.8	49.5	207.5	223.4	35.7	61.1	9.24	30.0	26.1	12.6	39.3	22.6
Ce	136.4	399.3	346.5	271.7	125.6	168.4	274.1	147.3	222.3	149.7	110.5	413.9	480.2	95.8	133.8	24.3	81.0	66.7	14.3	70.5	44.4
Pr	20.1	44.1	37.4	34.3	14.9	18.8	29.4	17.8	25.4	14.2	14.6	39.3	49.3	9.84	13.8	3.56	2.68	7.16	1.30	6.42	4.27
Nd	101.8	168.8	139.6	143.2	61.0	71.4	108.3	72.3	95.9	56.4	61.4	133.0	180.1	36.9	51.7	16.3	11.5	25.4	3.84	20.6	14.7
Sm	22.3	27.5	22.6	26.2	12.0	12.8	18.3	14.3	16.3	12.7	12.1	18.2	28.7	7.82	9.60	5.79	3.87	6.59	0.43	2.52	2.35
Eu	8.51	5.38	4.19	5.01	3.58	2.44	3.52	3.08	2.50	1.02	2.26	2.06	1.36	1.13	1.15	0.32	0.14	0.14	0.65	0.69	0.60
Gd	19.9	23.0	18.0	21.9	11.0	11.0	14.8	11.9	13.5	13.0	9.91	14.3	22.0	7.04	9.00	6.42	4.83	8.07	0.35	1.62	1.81
Tb	2.68	2.91	2.30	2.92	1.58	1.51	1.91	1.63	1.74	2.12	1.31	1.70	2.52	1.19	1.37	1.20	1.03	1.73	0.04	0.14	0.22
Dy	14.8	16.2	12.5	16.1	9.52	8.98	10.3	9.39	9.82	13.71	7.32	8.96	12.6	7.97	8.81	8.09	8.28	13.47	0.22	0.56	1.22
Ho	2.88	3.03	2.42	3.06	1.91	1.76	1.93	1.79	1.88	2.93	1.39	1.66	2.36	1.70	1.83	1.66	1.94	3.19	0.05	0.10	0.24
Er	7.90	8.24	6.74	8.25	5.27	4.91	5.10	4.81	5.13	8.71	3.75	4.44	6.59	5.19	5.42	4.74	6.37	10.7	0.15	0.31	0.73
Tm	1.21	1.15	0.92	1.17	0.77	0.70	0.66	0.66	0.71	1.34	0.51	0.60	0.97	0.82	0.84	0.68	1.07	1.96	0.03	0.05	0.11
Yb	9.58	7.51	6.26	7.66	5.41	4.53	4.16	4.30	4.65	9.44	3.31	3.83	7.04	5.81	5.76	4.37	7.96	14.1	0.21	0.35	0.86
Lu	1.79	1.05	0.88	1.06	0.78	0.62	0.55	0.58	0.63	1.28	0.47	0.53	1.05	0.83	0.82	0.58	1.08	1.97	0.04	0.06	0.13
Tl	0.22	0.53	0.61	0.51	0.86	0.91	0.74	0.64	0.15	1.32	0.82	0.52	0.39	1.05	0.59	0.13	1.10	1.30	0.42	0.59	0.52
Sb	0.01	0.01	0.04	0.01	0.07	0.04	0.02	0.02	0.03	0.08	0.04	0.06	0.03	0.05	0.11	0.09	0.17	0.07	0.03	0.04	0.05
A/CNK	0.6	0.9	0.9	0.9	1.0	1.0	1.0	1.0	1.0	1.0	1.6	0.9	0.9	1.1	0.9	1.4	1.1	1.0	1.1	1.1	1.0
A/NK	0.1	0.1	0.1	0.1	0.1	0.1	0.1	0.1	0.1	0.1	0.1	0.1	0.1	0.1	0.1	0.1	0.1	0.1	0.1	0.1	0.1
K_2O/Na_2O	0.8	1.3	1.2	1.5	1.4	1.7	2.0	1.7	0.1	1.7	2.2	1.9	1.2	1.8	0.9	8.1	1.3	1.1	1.5	1.1	0.9
Eu/Eu*	1.2	0.7	0.6	0.6	1.0	0.6	0.7	0.7	0.5	0.2	0.6	0.4	0.2	0.5	0.4	0.2	0.1	0.1	5.2	1.0	0.9
$(La/Yb)_N$	3.5	17.2	17.4	10.3	7.3	12.4	21.0	10.8	15.0	4.1	10.1	36.5	21.4	4.1	7.2	1.4	2.5	1.2	40.9	76.5	17.7
La/Th	81.4	31.7	13.0	30.7	4.7	8.2	14.5	27.6	12.4	2.6	10.0	7.3	13.7	1.7	2.7	0.6	1.3	0.6	26.1	2.7	2.2
Ce/Th	222	66.1	27.9	71.0	10.1	16.6	30.7	59.0	26.7	6.7	22.4	14.6	29.4	4.5	5.8	1.6	3.4	1.6	29.6	4.9	4.3
La/Nb	0.8	3.6	4.2	2.3	2.0	2.2	4.2	2.5	3.6	1.5	2.4	11.1	5.3	1.1	2.5	0.1	0.5	0.4	17.9	10.0	4.0
Zr/Hf	42.5	30.4	30.3	31.5	34.0	35.6	32.6	34.2	35.0	26.1	31.5	30.7	27.4	29.4	33.4	16.4	23.8	19.2	21.0	36.8	30.4
Y/Ho	23.3	25.5	24.9	24.7	23.2	24.9	23.3	23.2	23.8	24.4	23.9	22.2	24.8	24.1	23.9	16.3	20.1	27.4	19.7	25.7	25.0

Major element oxides in wt%. Trace element concentration in ppm by weight.

A/NK = Al/Na + K (molar prop); A/CNK = Al/Ca + Na + K (molar prop).

Geographic coordinate systems (GCS) in decimal degrees.

There is a peak in A-type granite production worldwide between 1500 and 1400 Ma, with large A-type batholiths in orogenic belts of Laurentia, eastern Grenville, Baltica, and in the Brazilian Shield (Bettencourt et al., 1999; Dall'Agnol et al., 1999; Condie, 2013, and references therein). Similarly, massif-type anorthosites are found in orogenic belts and are abundant during large parts of the Mesoproterozoic (e.g., Slagstad et al., 2018). Therefore, there may be a correlation between the production of A-type granites in the Mesoproterozoic and the formation of anorthosites in AMCG suites.

The Mesoproterozoic AMCG suite of the Kunene Complex of southern Angola and northern Namibia extends over > 15,000 km^2, and is one of the largest known AMCG suite on Earth (Bybee et al., 2019, and references therein). The Red Granite Suite is part of the Kunene Complex and forms approximately one-third of the exposed surface area (Fig. 1). In this study we use major and trace element compositions, U-Pb crystallization ages, and Lu-Hf isotopes in zircon to constrain the petrogenesis and tectonic setting of the Red Granite Suite. Our findings reveal that (i) the suite was emplaced over a prolonged timescale, similar to the Kunene anorthosites, that extends over 100 Myr (Bybee et al., 2019), and (ii) the Red Granite Suite magmas were produced from a mixture of juvenile mantle-derived melts and Paleoproterozoic crust. This study has important implications for the petrogenesis and tectonic setting of Mesoproterozoic A-type granites and AMCG suites.

2. Geological setting

2.1. Basement rocks to the Kunene AMCG Complex

The Paleoproterozoic and Mesoproterozoic eras are characterized by the development of major accretionary orogens across Laurentia, Baltica and Amazonia that formed during the assembly of the Columbia supercontinent between 2.4 and 1.3 Ga (e.g., Meert, 2012, Condie, 2013). The rocks that host the Mesoproterozoic Kunene AMCG Complex in southern Angola and northern Namibia (Fig. 1) are part of the Paleoproterozoic Lubango Zone crustal domain and correspond to the southern part of the Angolan Shield of Central Africa, along the present-day southwestern margin of the Congo Craton (Jelsma et al., 2018). An arc system developed along an active continental margin during the Paleoproterozoic in southern Angola and extended for 1000 km to the Kamanjab and Grootfonten inliers of Namibia in the south (Jelsma et al., 2018). At least three distinct magmatic events have been recognized over the region, which testify to the reworking of mainly Neoarchean crust, peaking at 2.0 Ga for the Eburnean granitoids in the north and extend to 1.77 Ga in the Epupa Metamorphic Complex in the south (Jelsma et al., 2018).

The western part of the Kunene Complex in Angola intruded a volcano-sedimentary sequence referred to as the 'schist, quartzite, and amphibolite complex' (de Carvalho and Alves, 1993), as well as a suite of Paleoproterozoic granites known as the Regional Granite. Regional Granite at the southwestern margin of the Kunene Complex has recently been dated at 1800–1780 Ma and is interpreted to be syntectonic with a regional deformation event (Lehmann et al., 2020). Regional Granite to the northwest of the Kunene Complex has older ages between 2050 and 1950 Ma (Pereira et al., 2011, McCourt et al., 2013), corresponding with the regional Eburnean magmatic event (Jelsma et al., 2018). The Regional Granite is unconformably overlain by the Chela Group, a sedimentary succession that forms the Humpata Plateau (Fig. 1), and that has been dated at ca. 1800 Ma (McCourt et al., 2013). The eastern margin of the Kunene Complex in Angola is concealed under Kalahari Group sediments.

The basement rocks to the Kunene Complex in northern Namibia are the Epupa Metamorphic Complex (Drüppel et al., 2007), which consists of prevalent migmatites and calc-alkaline orthogneisses dated at 1860–1760 Ma (Kröner et al., 2010, 2015). The migmatites of the Epupa Metamorphic Complex are divided into the metamorphosed supracrustal Eyao, Orue and Epembe units (Fig. 1, Brandt et al., 2003, 2007, 2021). Geochronological and petrological studies on these rocks indicate metamorphic events that are pre-, syn-, or post-Kunene emplacement (Seth et al., 2003, Seth et al., 2005, Brandt et al., 2021). The oldest HT-LP metamorphism is between 1740 and 1720 Ma in the Eyao Unit, and this was followed by Mesoproterozoic UHT metamorphism between 1520 and 1450 Ma in the Epembe Unit and then by upper amphibolite facies (lower-crustal conditions) metamorphism at ca. 1330 Ma in the Orue Unit peaking at 770 °C and 7.5 kbar (Seth et al., 2003, Seth et al., 2005, Brandt et al., 2003, Brandt et al., 2007, Brandt et al., 2021, Brandt and Klemd, 2008).

2.2. Kunene anorthosites

In Angola, the Kunene Complex is broadly N-S-trending and mainly consists of large bodies of anorthosite (*sensu stricto*) and associated leucotroctolite, leuconorite and leucogabbronorite (Ashwal and Twist, 1994, Drüppel et al., 2007, Bybee et al., 2019). In the Zebra Mountains of northern Namibia, the Kunene Complex forms a broadly E-W-trending antiformal structure and is composed of layers of olivine-bearing and pyroxene-bearing anorthosite (Maier et al., 2013). Recent high-precision ID-TIMS U-Pb zircon and baddeleyite dates for the Kunene anorthosites in Angola are between 1440 and 1375 Ma (Bybee et al., 2019). The same authors also dated an evolved pegmatoidal segregation in anorthosites in the central Angolan part of the Kunene Complex (Fig. 1) that had a significantly older age of 1500 ± 1.2 Ma. This suggests that the Kunene anorthosites were emplaced over a prolonged timescale of ≥ 120 Myr (Bybee et al., 2019). The Namibian part of the Kunene Complex anorthosite suite is comparatively poorly dated, with a single published U-Pb baddeleyite age of 1363 ± 17 Ma for olivine-bearing anorthosite along the Otjitanga River (Maier et al., 2013).

Mafic to ultramafic intrusions, mainly composed of dunite, harzburgite, pyroxenite, troctolite, gabbro, with minor anorthosite, occur as irregular stocks along the western and southern margins of the Kunene Complex. These have been described as satellite intrusions to the main Kunene Complex and have the potential to host Ni-Cu-(Co)-PGE mineralization (Ashwal and Twist, 1994, Maier et al., 2013).

The thermobarometric conditions for the emplacement of the Kunene anorthosites are not yet well constrained, and different P-T conditions come from studies in the southern and northern portions of the complex. Lower crust conditions (7–9 kbar) have been estimated from Ti-in-amphibole barometry in anorthosite in the Zebra Mountains (Drüppel et al., 2001). However, Slejko et al. (2002) suggested shallow-level crystallization (3–5 kbar), estimated using clinopyroxene-orthopyroxene equilibration temperatures of 880 °C in a sample of anorthosite from the northern portion of the Kunene anorthosites in Angola.

2.3. Red Granite Suite

The felsic part of the Kunene AMCG Complex is referred to as the Red Granite Suite, and includes dominant granite and granite porphyry, as well as mangerite, charnockite, granodiorite, syenite, monzonite (Fig. 1). The Red Granite Suite is in contact with Kunene

Complex anorthosites, crystalline basement, and metamorphosed supracrustal rocks (de Carvalho and Alves, 1993, McCourt et al., 2013, Lehmann et al., 2020).

In the north of the Kunene Complex, the Red Granite Suite forms a NNE–SSW-trending belt that divides the Kunene anorthosites of Angola into two distinct compositional regions (Morais et al., 1998, Mayer et al., 2004). Large portions of granite crop out in the northeastern sector of the Kunene Complex in the Matala region (partly shown in Fig. 1) and substantial exposures are also present to the west in the Ompupa region. The Red Granite Suite forms a large part of the southern Kunene Complex in Angola, with extensive exposures to the SE and W of the anorthosites. In Namibia, granitoids purportedly similar to the Red Granite Suite intruded the Epupa Metamorphic Complex as ENE–WSW-elongated bodies and are exposed at the western and southeastern margins of the Zebra Mountains (Drüppel et al., 2007, Brandt and Klemd, 2008).

Field evidence and Rb-Sr age dating indicate that the Red Granite Suite is coeval or younger than the anorthosites (Torquato et al., 1979, de Carvalho et al., 1987, de Carvalho and Alves, 1990, Morais et al., 1998). U-Pb zircon dating of the granitoids yielded a date at 1371.3 ± 2.5 Ma for a mangerite dyke cross-cutting anorthosite near Dongue in the northern Kunene Complex (Mayer et al., 2004) and a SHRIMP U-Pb zircon date for the same dyke at 1385 ± 7.6 Ma (McCourt et al., 2013). Seth et al. (2005) provided a SHRIMP U-Pb zircon date of 1374.0 ± 5.2 Ma for a weakly foliated granite from an ENE–WSW-trending felsic intrusive belt hosted by the Orue Unit on the southern margin of the Kunene Complex. In the same area, Kröner and Rojas-Agramonte (2017) provided a date of 1214 ± 3 Ma on a coarse-grained porphyritic granite. The link between the latter rock and the Red Granite Suite is unclear as there is also an alkaline suite distributed within the gneisses of the Epembe Unit described by Ferguson et al., 1975, Menge, 1986 and which was dated at ca. 1215 Ma (U-Pb zircon; Littmann et al., 2000). A few kilometers to the north in the Zebra Mountain anorthosites, Drüppel et al. (2007) dated an undeformed syenodiorite, which forms part of a swarm of syenites, at 1376 ± 2 Ma. The most recent U-Pb zircon dating of the Red Granite Suite produced dates between 1450 and 1370 Ma in the southwestern parts of the Kunene Complex in Angola (Lehmann et al., 2020).

SHRIMP U-Pb zircon dates at 1521.6 ± 1.5 Ma and 1533.5 ± 1.2 Ma have been recorded on two undeformed granitoids (granodiorite and granite, respectively) approximately 50 km west of the Zebra Mountains (Kröner et al., 2015). Based on field observations, it was suggested that these granitoids were derived from anatectic melting of a Paleoproterozoic protolith related to a major thermal event in this area at ca. 1520 Ma (Kröner et al., 2015). Such relatively old dates have not been recognized elsewhere in the Red Granite Suite and their significance remains uncertain.

To the west and east of the Zebra Mountains along the Kunene River, as well as further to the southwest in Kaokoland, there are 1440 and 1350 Ma metaluminous to peraluminous granitoids that have been deformed with the Epupa rocks (Seth et al., 2005, Drüppel et al., 2007, Kröner and Rojas-Agramonte, 2017). These rocks may share a genetic relationship with the Kunene Complex.

2.4. Tectonic setting for the Kunene Complex

The emplacement of the Kunene Complex has previously been attributed to a period of significant crustal extension and the presence of a large thermal anomaly below the southern margin of the Congo Craton (Mayer et al., 2004, Drüppel et al., 2007, McCourt et al., 2013, Kröner and Rojas-Agramonte, 2017, Jelsma et al., 2018). The reasons for such extension are debated, however, it is noteworthy that the timing of the Kunene Complex emplacement overlaps with the ca. 1375 Ma 'Kibaran' magmatic event, 2100 km to the northeast, in the Karagwe-Ankole Belt of Central Africa (Tack et al., 2010). The synchronicity of these events has been invoked to support the presence of a Large Igneous Province (LIP), active at 1.38 Ga for a relatively short time along the margins of the Greater Congo Craton (Ernst et al., 2013, Mäkitie et al., 2014, Blanchard et al., 2017).

The LIP model is debated for both the Karagwe-Ankole Belt and the Kunene Complex on structural and geochronological grounds. In the former, $^{40}Ar/^{39}Ar$ dates at 1350–1326 Ma of orogenic fabrics are interpreted to mark continental collision (Koegelenberg et al., 2015). In the latter, Lehmann et al. (2020) present new data from the southwestern margin of the Kunene Complex in Angola, which show that the Red Granite Suite and the Kunene anorthosites in this area were emplaced during E-W contraction between 1400 and 1380 Ma. The evidence for this regional contraction event, plus the long duration of Kunene anorthosite magmatism, led Lehmann et al. (2020) to propose a contractional setting for the Kunene Complex, in agreement with recent understanding of the petrogenesis of Mesoproterozoic anorthosites and related rocks (Ashwal, 2010, Ashwal and Bybee, 2017). During the Neoproterozoic and Cambrian, the country rocks to the west of the KC were involved in the Araçuaí-West Congo orogeny, which resulted from collision of the Congo Craton with the eastern margin of the São Francisco Craton (Alkmim et al., 2006).

3. Methods

In this paper, we use the geochemistry and geochronology of the Red Granite Suite as a basis to investigate the petrogenesis and disputed tectonic setting for the Kunene Complex. We selected 28 samples from the Red Granite Suite, and six from the Paleoproterozoic basement from Angola, including five granitoids from the Regional Granite and one anorthosite from a mafic intrusion hosted in Regional Granite. The anorthosite sample is part of the Paleoproterozoic Caongoquepia mafic intrusion (Angola), which intrudes the Regional Granite approximately 25 km west of Pocolo (Langa, 2019). The Red Granite Suite samples are widely distributed, covering an area of ca. 200 × 60 km in Angola, and extending from the NNE-SSW-trending granite belt to the extensive outcrops of granite in the southernmost part of the Kunene Complex (Fig. 1). Twenty-one Red Granite Suite rocks were analyzed for major and trace elements at the University of Pretoria (XRF) and the University of the Witwatersrand (ICP-MS). Zircon grains were separated from seven representative samples of the Red Granite Suite and from five samples of the Paleoproterozoic basement and were dated by the U-Pb method using a Nu Plasma HR LA-MC-ICPMS at the University of Johannesburg. Hf isotopes in zircon were analyzed on the same instrument in 20 dated samples from this study and for part of the samples presented in Lehmann et al. (2020). Detailed analytical methods are reported in the supplementary material.

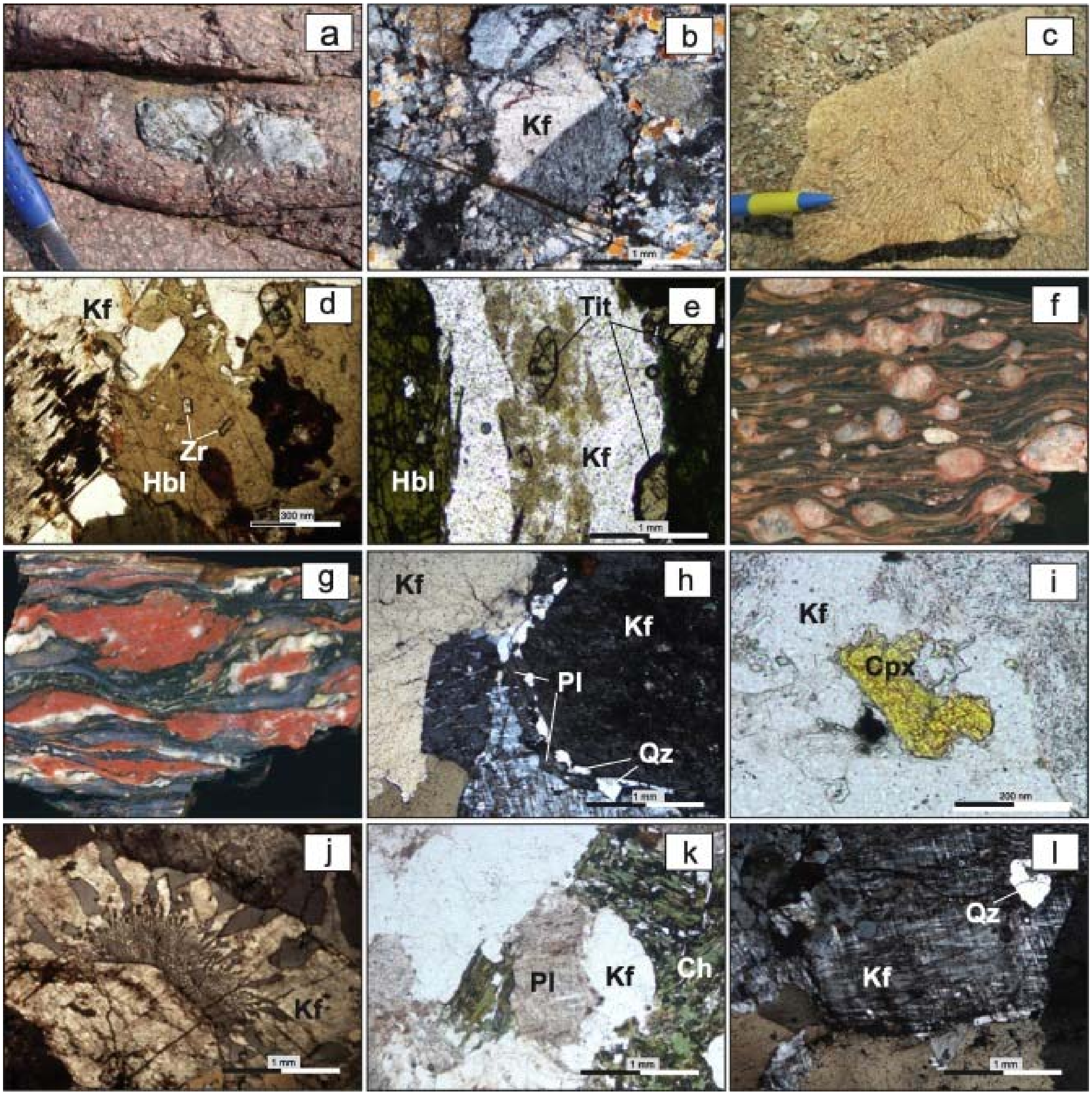

Fig. 2. Representative field photographs and photomicrographs of the Red Granite Suite. a) Medium-grained syenitic gneiss KAC234-235 enclosing a rounded anorthosite xenolith. b) Carlsbad twinning in perthitic K-feldspar in granite KAC297. Sub-parallel late hydro-oxide veinlets are also visible (XPL). c) Cuneiform intergrowth of quartz and K-feldspar (graphic texture) in bimineralic leucogranite KAC45-46. d) Hornblende oikocryst including numerous prismatic zircons in qz monzonite KAC260-254 (PPL). e) Euhedral titanite crystals in mylonitic qz monzonite KAC32-236 (PPL). f) Megacrystic mylonite KAC23-28B with relict augens of K-feldspar rimmed by plagioclase and set in a dark hematized foliated groundmass. g) Protomylonite KAC331-1 showing flattened K-feldspar augens in a foliated groundmass in light (quartz + K-feldspar) and dark (amphibole-rich) mm-scale bands. h) Possible localised rapakivi texture around K-feldspar megacryst, qz monzonite KAC260-254 (XPL). i) Green-yellow pleochroic, moderate relief, Na-pyroxene (likely aegirine) in K-feldspar, qz monzonite 34-37B (PPL). j) Radial myrmekite development in K-feldspar, granite KAC31-35 (PPL). k) Saussuritized plagioclase and K-feldspar intergrowth with chloritized hornblende oikocryst. Qz monzonite KAC34-37B (PPL). l) Microcline crystal with rounded inequigranular quartz inclusions in granite KAC61-58 (XPL). Ch = chlorite; Cpx = clinopyroxene; Hbl = hornblende; Kf = K-feldspar; Pl = plagioclase; Qz = quartz; Tit = titanite; Zr = zircon.

4. Results

4.1. Mineralogy and petrography of the Red Granite Suite

The granitoids and gneisses of the Red Granite Suite have grain sizes ranging from coarse-grained (porphyritic to megacrystic) to fine-grained, can be divided into undeformed or deformed (up to ultramylonite) varieties, and have a typical reddish color due to the presence of disseminated iron oxides. The studied samples are mostly silica-oversaturated granites, with minor quartz monzonites and syenites. A meter-wide mylonite sheet (KAC208-205) and a 50-cm wide undeformed vein (KAC221-219) injected into the Paleoproterozoic basement were also sampled. Field photographs and microphotographs of the main phases and representative textures for the granitoid samples are reported in Fig. 2a-l.

The undeformed Red Granite Suite samples are medium- to fine-grained and have porphyritic to megacrystic textures. Round to subangular dm-scale anorthosite xenoliths sporadically occur and suggest there was felsic magma emplacement into Kunene anorthosite (e.g., KAC34-37B, KAC234-235: Fig. 2a). The megacrystic granites are characterized by large (up to 5 cm) euhedral grains of Carlsbad-twinned K-feldspar (Fig. 2b). Some leucocratic granites show outcrop-scale graphic intergrowths of quartz and K-feldspar (KAC45-46: Fig. 2c). Biotite is ubiquitous among the ferromagnesian accessory minerals and hornblende may be locally abundant (e.g., KAC61-58) as mm-size elongated euhedral/subhedral crystals. Magnetite and ilmenite make up most of the opaque phases. Rutile, apatite, monazite, and zircon are common accessory minerals (e.g., KAC260-254: Fig. 2d). Titanite (mm-sized) may be abundant (e.g., KAC32-236: Fig. 2e).

The deformed Red Granite Suite samples are fine- to medium-grained and have megacrystic gneissose to ultramylonite textures. Dynamic recrystallization and grain size reduction produced mylonitization in some of the samples (KAC23-28B, KAC32-236, KAC234-235, KAC331-1: Fig. 2f, g), with local ultramylonites also present (e.g., KAC23-28C and KAC230-233). Centimeter-scale K-feldspar augen porphyroclasts (±medium-grained hornblende) are set in a matrix of recrystallized quartz ribbons, feldspar, and biotite (±amphibole), locally developing compositional layering. Late-stage hydrothermal oxides can produce homogeneous staining as micro-veinlets oriented parallel to the main gneissic foliation.

Rapakivi textures are present in some of the granitoids (e.g., KAC260-254, Fig. 2h), but the overall proportion of rocks characterized by plagioclase-mantled K-feldspar is scarce. Rare (sodic?) pyroxene is present in the quartz monzonites (mangerite) (e.g., KAC34-37B: Fig. 2i). Other common textures (including myrmekite) in the Red Granite Suite are shown in Fig. 2j-l.

4.2. Major and trace element compositions of the Red Granite Suite

Major and trace element compositions of 21 Red Granite Suite samples are presented in Table 1. Eleven of the samples represent deformed rocks. Full details of the analytical techniques are given in the supplementary material.

The samples are evolved felsic rocks (59.1–76.7 wt% SiO_2; see Table 1). The rocks range from syenite to quartz monzonite to granite and are mostly sub-alkaline (Fig. 3a, b). Loss on ignition (LOI) values (up to 1.5 wt%) indicate a low volatile content and limited alteration, even in highly deformed samples (i.e., ultramylonites). The samples show progressive depletion in TiO_2, Al_2O_3, FeO_{tot}, MgO, CaO, and P_2O_5 with increasing silica content. The rocks are potassic (apart from KAC23-28C, according to the definition $Na_2O-2 < K_2O$), with $Na_2O + K_2O$ content ranging from 6.3 to 9.9 wt%. Al_2O_3 ranges between 11.9 and 16.0 wt%. The most evolved (75.3–76.7 wt% SiO_2) samples are characterized by bimineralic quartz + K-feldspar mineral assemblages (e.g., KAC43-45, KAC45-46, KAC269-269 and KAC297). The lack of biotite and amphibole is consistent with the low TiO_2, FeO_{tot}, MnO, MgO and P_2O_5 contents of these samples. Most samples plot within the alkali-calcic and alkalic fields on a MALI diagram, however, a few samples plot in the calc-alkalic field, suggesting that there is source heterogeneity (Fig. 3c). A ferroan-type character is evident from the FeO/(FeO + MgO) versus SiO_2 discrimination diagram of Frost and Frost, 2008, Frost and Frost, 2011, although some of the most evolved samples show magnesian affinities (Fig. 3d), and most samples are metaluminous (Fig. 4).

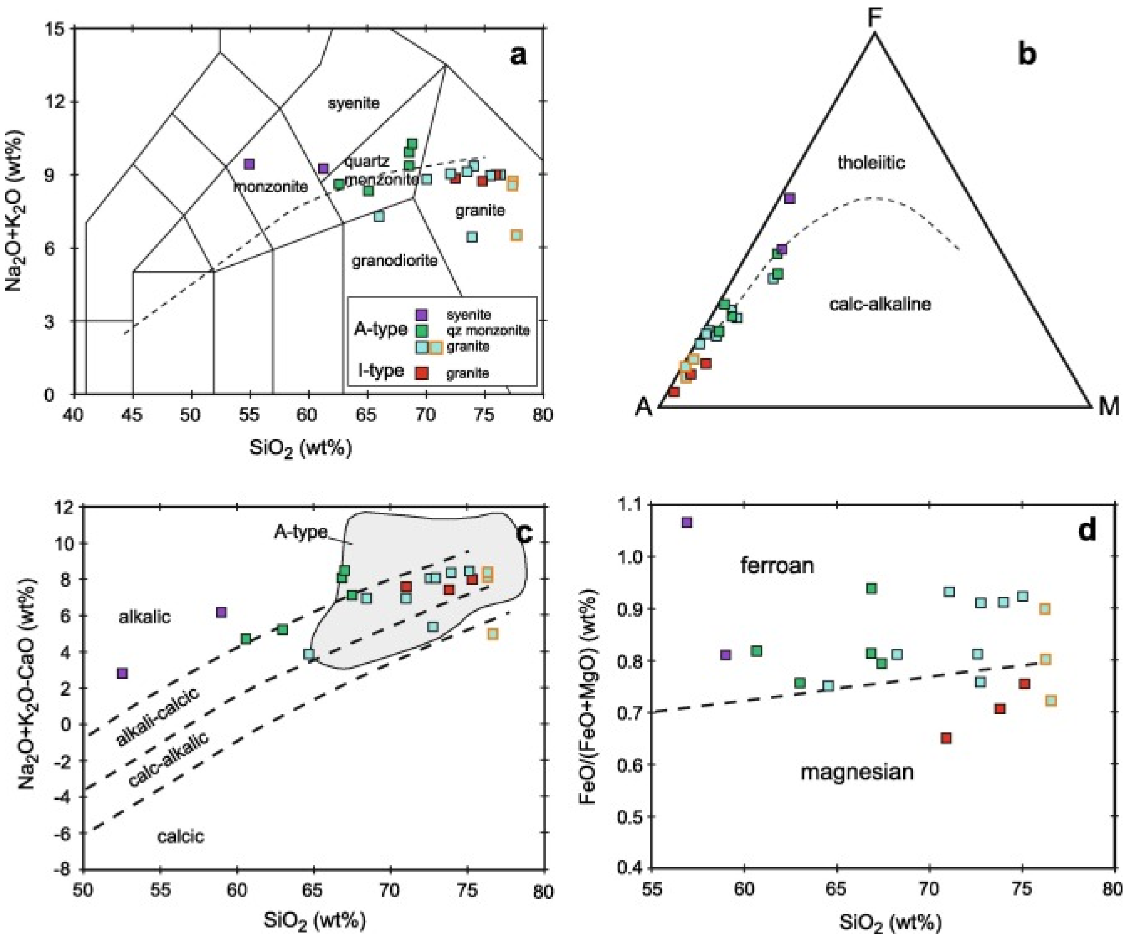

Fig. 3. Chemical classification diagrams for representative Red Granite Suite rocks. a) Total alkali-silica (TAS) diagram adapted to plutonic rocks (after Middlemost, 1994); symbols and colors as in the legend. Symbols with an orange border refer to granites showing a tetrad effect in REE (see text); the dashed line separating alkaline from subalkaline series is after Irvine and Baragar (1971). b) AFM diagram, after Irvine and Baragar (1971). c) Alkali-lime (MALI) index ($Na_2O + K_2O-CaO$) (Frost and Frost, 2011) vs. SiO_2 diagram. A-type granite

composition of Lachlan Fold Belt is from Frost and Frost (2011), and references therein. d) FeO/(FeO + MgO) vs. SiO_2 diagram discriminating between ferroan and magnesian granitoids (Frost and Frost, 2011).

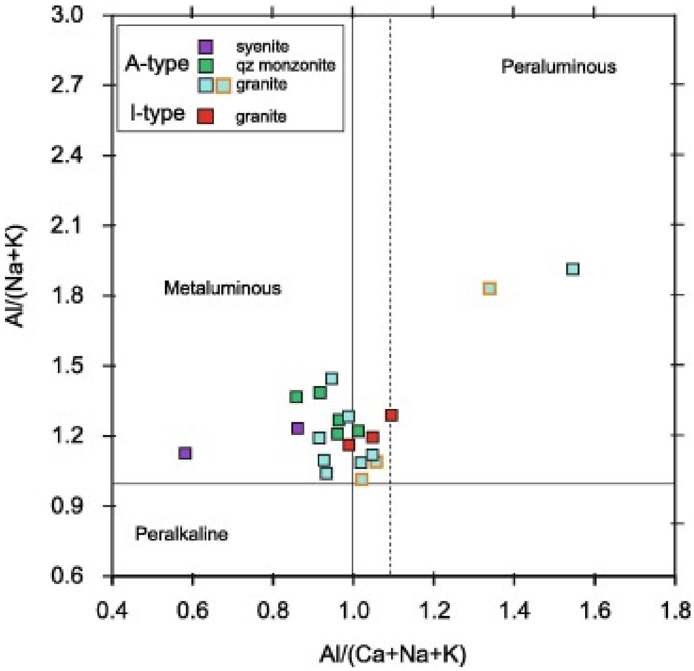

Fig. 4. A/NK [molar ratio $Al_2O_3/(K_2O + Na_2O)$] vs. A/CNK [molar ratio $Al_2O_3/(CaO + Na_2O + K_2O)$] diagram of granitoids, after Maniar and Piccoli (1989).

The primordial mantle (PM)-normalized distribution shows variable, but relatively high contents of large ion lithophile elements (LILE) and rare earth elements (REE; specifically, La, Ce, Nd, Sm and Tb) and negative anomalies in Sr, P and Ti (which are most pronounced in the granites) (Fig. 5a, b). Such depletion is most prominent in the samples with the highest SiO_2 contents (SiO_2 > 76 wt%; KAC45-46, KAC269-269, KAC297), which also record the lowest Fe, Mn, and Mg contents. U (up to 6.3 ppm) and Th (up to 38.5 ppm) concentrations are generally low, with variable Pb concentrations (4.6 and 32.6 ppm), and there is a progressive increase in U/Pb from syenite (ca. 0.10) to granite (up to 0.67).

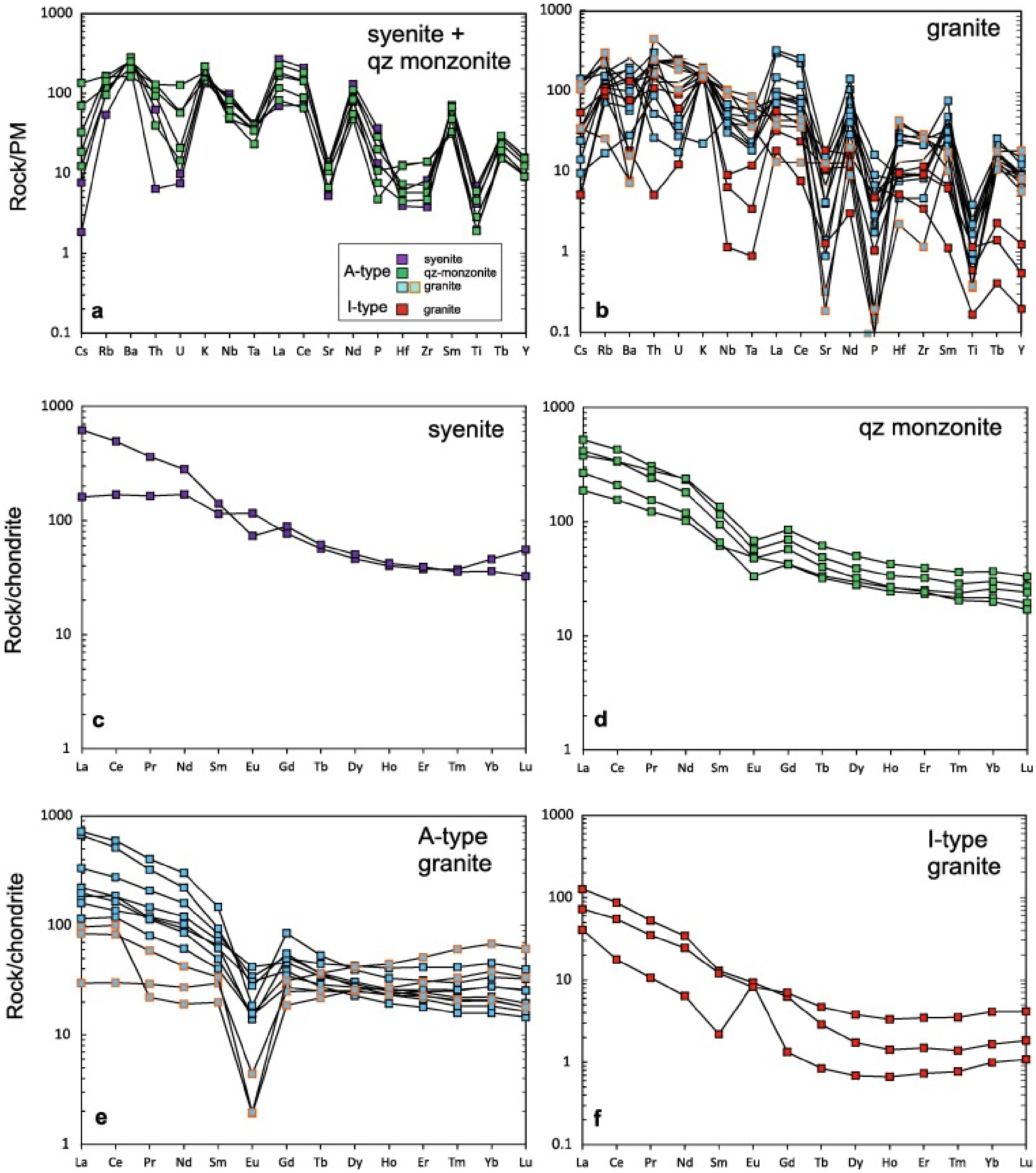

Fig. 5. Primitive mantle-normalized trace element diagram (a, b) and chondrite-normalized rare earth element patterns (c-f) for the studied rocks. Primitive mantle normalizing values after Wood et al. (1979); chondrite values after Boynton (1985). Squares with orange border (e): evolved granites showing the tetrad effect (KAC45-46, KAC269-269 and KAC297).

Chondrite-normalized REE patterns are moderately steep, with a general decrease in LREE and MREE from syenite to monzonite to granite (Fig. 5c-f). The highest REE concentrations are recorded in granite KAC186-188, which also contains abundant monazite. Except for the syenite (KAC79-74), the samples show negligible to marked depletion in Eu (e.g., Eu/Eu* = 0.06–0.95, with $Eu/Eu^* = (Eu)_N/[(Sm)_N \times (Gd)_N]^{0.5}$) that reflects a variable extent of feldspar fractionation. $(La/Yb)_N$ is variable (1.24–36.5), but the lowest $(La/Yb)_N$ values (1.24–2.54) are recorded in the three most evolved samples (KAC45-46, KAC269-269, KAC297, with SiO_2 > 76 wt%, squares with orange border in Fig. 5e). These samples are also peraluminous, show HREE enrichment, a REE M−type tetrad effect (Masuda et al., 1987), are depleted in Ba, Sr, P, Ti, Eu, and show low Zr/Hf, La/Th, Ce/Th, and high Nb, Ta, U and Th (Fig. 5b, e).

Some of the Red Granite Suite samples show a marked depletion in Nb, Ta, Zr, Ti, Y and REE, with a steep trend from LREE to MREE and a flat HREE distribution (e.g., KAC43-45, KAC208-205 and KAC221-219, red squares in Fig. 5b, f).

4.3. Geochronology

U–Pb zircon dates were determined for seven Red Granite Suite samples, four Regional Granite samples, and an anorthosite sample from the Paleoproterozoic Caongoquepia mafic intrusion within the Regional Granite (Fig. 1, Table 2 and supplementary material). Red Granite Suite dates were obtained from both undeformed and deformed granites and an undeformed quartz monzonite. Table 2 includes our dates (Red Granite Suite and basement rocks) and all U-Pb dates for the Red Granite Suite that we have obtained from the literature. The results for the granitoid suite can be grouped into 3 age ranges, (i) 1450–1410 (n = 3), (ii) 1400–1380 (n = 6), and (iii) 1380–1360 Ma (n = 9) (Table 2). Representative zircon cathodoluminescence (CL) images are in Fig. 6 and graphic results are in Fig. 7. Zircon habits and textures for each sample are in the supplementary material along with the U-Pb data in Table 1SM.

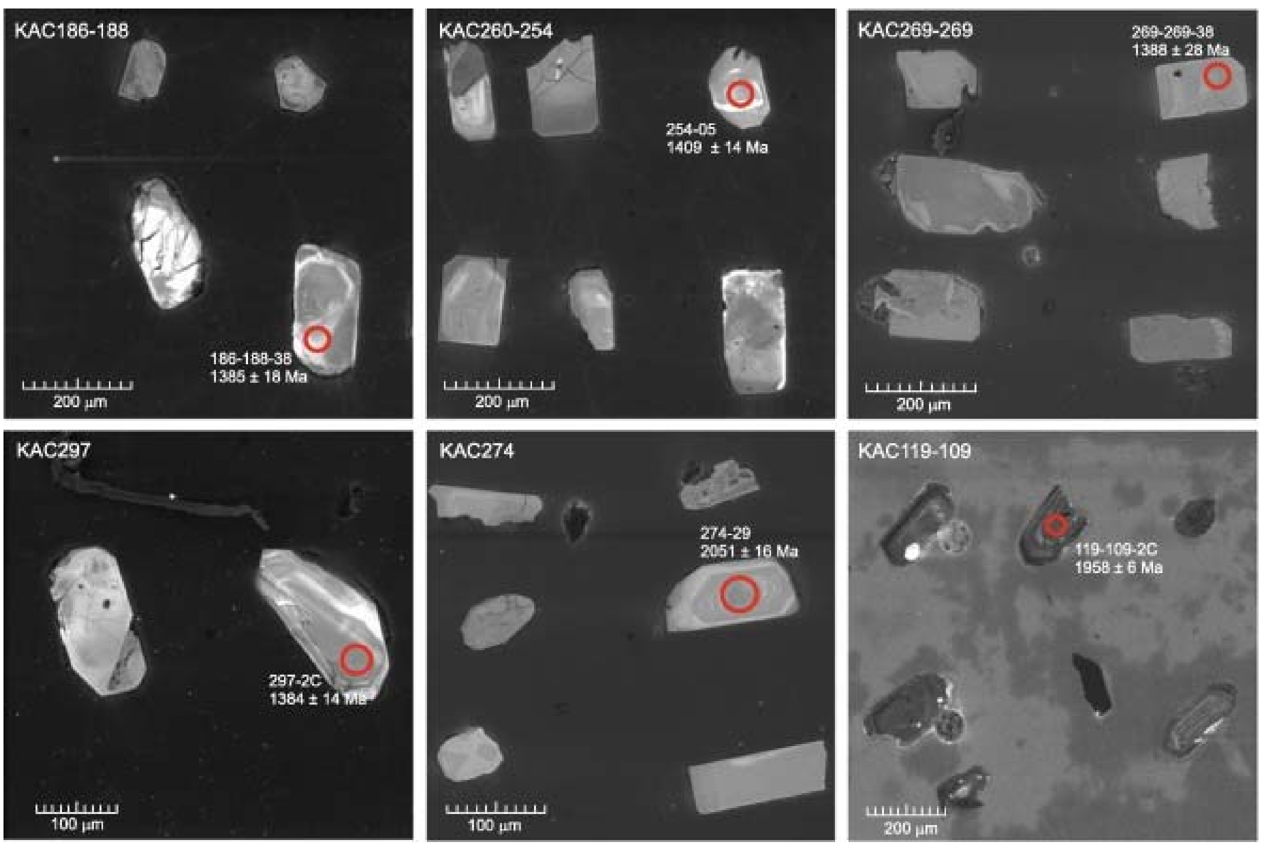

Fig. 6. Cathodoluminescence images of representative zircon grains from the Red Granite Suite and Regional Granite KAC119-109. The positions of laser spots are indicated. Dates refer to $^{207}Pb/^{206}Pb$ (full data in Table 1 in supplementary material).

Table 2. Compilation of zircon chronological results for the Red Granite Suite belonging to the Kunene Complex, divided according to age range. The recent dates of the basement rocks are also reported. Locations are from GPS acquisition, except for Ku-98–201, 180–1 and 'Mangerite dyke', extrapolated from map in publications.

Sample	Long E (dec deg)	Lat S (dec deg)	Rock type	Date range	Date	2 s	Type	MSWD	Method	Interpretation	Reference
Red Granite Suite											
KAC43-43	13.678043	16.550546	Megacrystic augen gneiss	**1450–1410**	1442	8	weighted mean	5	U-Pb LAMCICPMS	CA	Lehmann et al. (2020)
KAC274	13.635403	17.086877	Fine-grained granite		1441	3	concordia	1.6	U-Pb LAMCICPMS	CA	this work
KAC260-254	13.708975	15.923305	Megacrystic qz monzonite		1414	4	concordia	1.4	U-Pb LAMCICPMS	CA	this work
KAC23-28A	13.485900	16.781190	Megacrystic augen gneiss	**1400–1380**	1391	9	weighted mean	1.1	U-Pb LAMCICPMS	CA	Lehmann et al. (2020)
KAC34-37A	13.441027	16.681810	Megacrystic granite gneiss		1393	7	upper intercept	1.5	U-Pb LAMCICPMS	CA	Lehmann et al. (2020)
KAC35-38B*	13.449689	16.593061	Fine-grained dark microgr in KAC35-38A		1391	14	weighted mean	3.9	U-Pb LAMCICPMS	CA	Lehmann et al. (2020)
KAC301-01	13.362436	16.962940	Fine- to medium-grained gneiss		1392	5	concordia	0.8	U-Pb LAMCICPMS	CA	this work
KAC35-38A	13.449689	16.593061	Fine-grained granite gneiss		1387	8	upper intercept	3.1	U-Pb LAMCICPMS	CA	Lehmann et al. (2020)
KAC61-58	13.923343	16.499553	Medium-grained granite		1386	5	concordia	1.6	U-Pb LAMCICPMS	CA	this work
KAC31-35	13.469986	16.941510	Medium-grained granite	**1380–1360**	1380	5	upper intercept	2.4	U-Pb LAMCICPMS	CA	Lehmann et al. (2020)
KAC297	13.538857	17.075111	Medium-grained granite		1377	4	concordia	1.9	U-Pb LAMCICPMS	CA	this work
Ku-98–201	13.824656	17.377885	Syenodiorite		1376	2	upper intercept	0.4	U-Pb TIMS	CA	Drüppel et al. (2007)
Na190	14.033250	17.423083	Weakly foliated granite		1375	4	concordia	–	U-Pb SHRIMP	CA	Kröner and Rojas-Agramonte (2017)
KAC269-269	13.889764	15.595566	Granite gneiss		1374	10	upper intercept	1.2	U-Pb LAMCICPMS	CA	this work
180–1	13.767391	17.431773	Fine- to medium-grained granite		1373	6	upper intercept	1.0	U-Pb SHRIMP	CA	Seth et al. (2005)
KAC43-44	13.678043	16.550546	Microgranitic dike		1372	5	upper intercept	2.0	U-Pb LAMCICPMS	CA	Lehmann et al. (2020)
Mangerite dyke	14.005912	15.415038	Mangerite dyke		1371	3	upper intercept	1.2	Pb-Pb evap.	CA	Mayer et al. (2004)

KAC186-188	14.081797	15.414246	Granite gneiss		1370	9	concordia	1.5	U-Pb LAMCICPMS	CA	this work
Basement rocks											
KAC27-31	13.463860	16.904320	Granodiorite gneiss		1782	9	weighted mean	0.5	U-Pb LAMCICPMS	CA	Lehmann et al. (2020)
KAC74-71	13.935498	15.837491	Granodiorite		1947	4	concordia	1.5	U-Pb LAMCICPMS	CA	this work
KAC98-92	14.037250	14.945120	Granite		1830	27	upper intercept	1.5	U-Pb LAMCICPMS	CA	this work
KAC119-109	14.425314	14.800068	Granite		1964	3	concordia	0.9	U-Pb LAMCICPMS	CA	this work
KAC254-250	13.452443	16.874024	Granodiorite sill		1800	5	upper intercept	0.7	U-Pb LAMCICPMS	CA	this work
KSAT35-22	13.558591	15.784633	Anorthosite		1780	11	concordia	1.9	U-Pb LAMCICPMS	CA	this work

Geographic coordinate systems (GCS) in decimal degrees. CA = crystallization age.

*the attribution of KAC35-38B (micrograite in KAC35-38A) as part of the RGS is unclear.

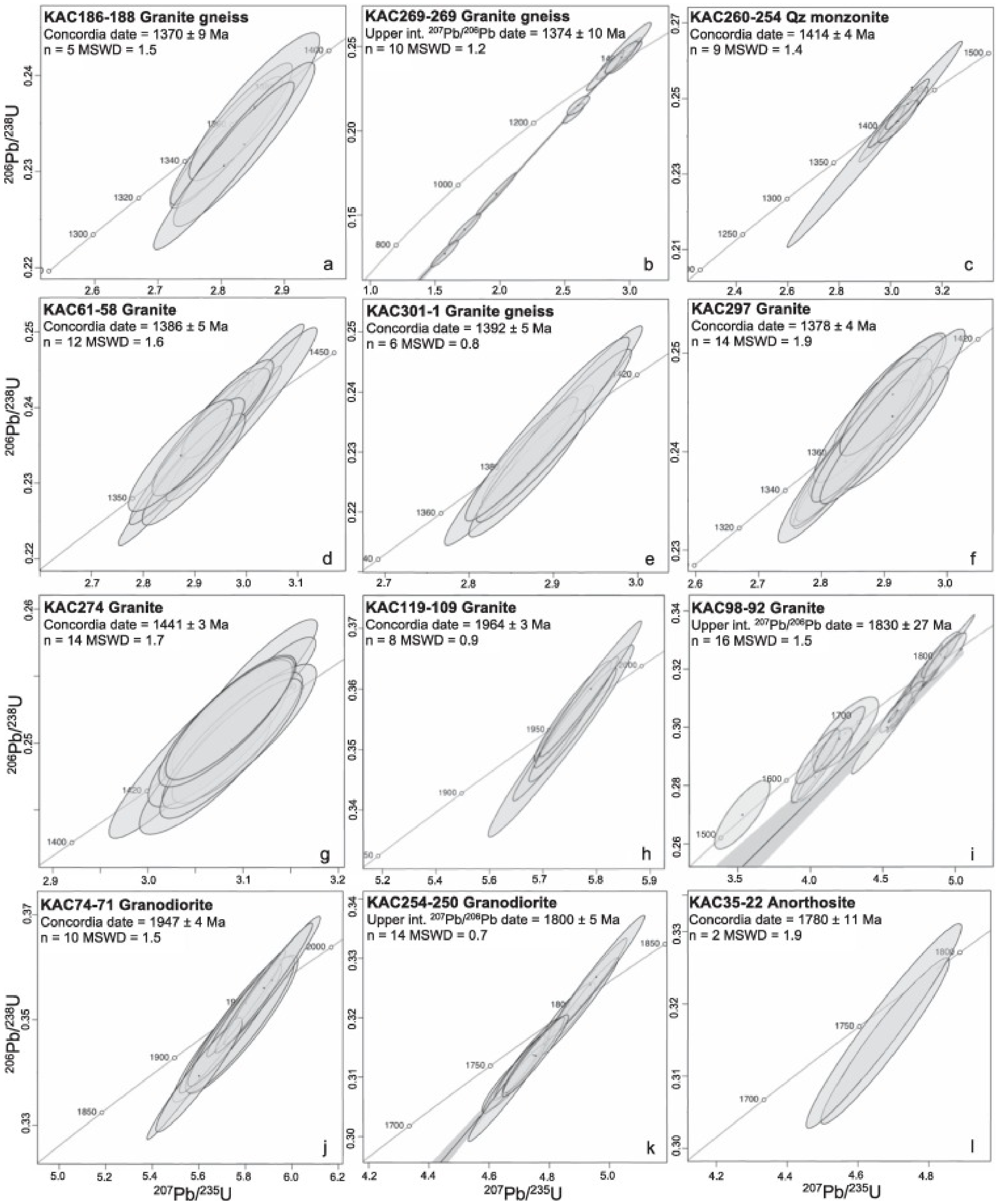

Fig. 7. LA-ICP-MS zircon U–Pb results shown in Wetherill concordia diagrams. Data point error ellipses are 2σ. The concordia ages are calculated at the 95% confidence level. MSWD is the mean square of weighted deviates for combined equivalence and concordance of the data points used for the age calculation. The data were processed and plotted using Isoplot software (Ludwig, 2003).

4.3.1. Geochronology of the Red Granite Suite

The geochronology results for our samples are listed from north to south. KAC186-188 is a medium- to fine-grained granite gneiss from the northernmost part of the NNE-SSW-trending granitic belt characterized by dominant quartz (partially recrystallized), sericitized K-feldspar, and minor plagioclase with scarce biotite and diffuse staining by Fe-oxide/hydroxide. Five analyses on five zircon grains (one analysis per grain) plot on a concordia and give a date interpreted as a crystallization age of 1370 ± 9 Ma (concordance & equivalence MSWD = 1.5) and a weighted mean $^{207}Pb/^{206}Pb$ age of 1365 ± 9 Ma (six zircons, MSWD = 2.2).

KAC269-269 is a porphyritic red granite gneiss from the NNE-SSW granitic belt and is composed mostly of quartz and minor feldspar present as porphyroclasts wrapped in a mylonitic foliation of recrystallized quartz and abundant Fe-hydroxide. Three analyses on three zircon grains plot on a concordia and give a poorly constrained date of 1375 ± 17 Ma (MSWD = 1.8), which we consider to be the crystallization age. The precision of this age slightly improves considering ten grains that plot on a discordia (upper intercept) and provide an age of 1374 ± 10 Ma (MSWD = 1.2).

KAC260-254 is an undeformed megacrystic quartz monzonite sampled in the southernmost sector of the NNE-SSW-trending granitic belt and characterized by large feldspar phenocrysts (up to 2 cm long), quartz and minor plagioclase. Microcline is highly sericitized and the abundant amphibole is typically intergrown with biotite and rimmed by Fe-hydroxide (limonite). Prismatic zircon and apatite are abundant as inclusions in hornblende (e.g., Fig. 2d). Nine concordant grains yield a date of 1414 ± 4 Ma (MSWD = 1.4), interpreted as a crystallization age, and 12 zircons provide a weighted mean $^{207}Pb/^{206}Pb$ age of 1414 ± 4 Ma (MSWD = 2.2).

Sample KAC61-58 is an undeformed medium-grained granite from the extensive region of Red Granite located to the SE of the Angolan Kunene Complex. The sample has significant perthitic feldspar and quartz associated with plagioclase, biotite, anhedral large dark-green amphibole, and opaque minerals. Twelve analysis spots on 12 zircon grains plot on a concordia and yield an age of 1386 ± 5 Ma, which is interpreted as the crystallization age (MSWD = 1.6). The sample yields a weighted mean age of 1384 ± 4 Ma (29 grains, MSWD = 1.5).

KAC301-1 is a fine- to medium-grained granite gneiss that was sampled in the southwesternmost sector of the Angolan Kunene Complex. Elongated mm-wide lenses of quartz are wrapped in a matrix of subparallel bands, where recrystallized and elongated quartz and feldspar are present as sub-tabular grains that alternate with laths of bent and recrystallized hornblende. Six analyses (on 6 zircon grains) are concordant and give a date, which we assume to represent the crystallization age, of 1392 ± 5 Ma (MSWD = 0.8), with a weighted mean age of 1392 ± 5 Ma (8 grains, MSWD = 0.8).

KAC297 and KAC274 were sampled in the southernmost Angolan part of the Kunene Complex. In hand specimen, KAC 297 is an undeformed medium-grained leucogranite characterized by subhedral K-feldspar grains in a matrix of recrystallized quartz and oxides as stockwork veinlets. Microscopically, K-feldspar grains show lobate contacts, core and mantle structures, and quartz is recrystallized, indicating incipient crystal plastic deformation. Fourteen analyses (on 14 grains) provide a concordant age of 1378 ± 4 Ma (MSWD = 1.9), which we interpret as the crystallization age, with a weighted mean age of 1378 ± 4 Ma (17 grains, MSWD = 1.5).

KAC274 is an undeformed fine-grained granite characterized predominantly by microgranular quartz and K-feldspar, with rare biotite as tabular elongated grains. The rock is reddish due to the abundance of limonite as subparallel bands, cut by late-stage subparallel veinlets also filled with Fe-(oxy-)hydroxides. Fourteen analyses (on 14 zircon grains) provide a concordant date of 1441 ± 3 Ma (MSWD = 1.7) interpreted as a crystallization age, and a weighted mean age of 1442 ± 3 Ma (17 grains, MSWD = 0.8). Two minor xenocrystic populations were also found, with 2 grains yielding $^{207}Pb/^{206}Pb$ concordant dates of 1790–1770 Ma and 4 grains yielding a date of ca. 2050 Ma (Table 1SM, supplementary material).

4.3.2. Geochronology of the basement rocks

The basement rocks of the Regional Granite (Fig. 1, Fig. 7 and Table 2) are medium- to coarse-grained, granitic to granodioritic in composition. Zircons are well-preserved, prismatic, with regular oscillatory zoning. Xenocrystic cores are common (see supplementary material).

KAC119-109 is a porphyritic granite in the basement to the north of the Kunene Complex. Eight analyses (on 8 zircons) provide a concordia date of 1964 ± 3 Ma (MSWD = 0.9), which we consider to be the crystallization age, with a weighted mean $^{207}Pb/^{206}Pb$ age of 1968 ± 3 Ma (15 grains, MSWD = 2.9).

KAC98-92 is a massive coarse-grained granite from the basement to the northwest of the Kunene Complex. Sixteen analyses (on 13 zircons) plot on a discordia line and yield a date of 1830 ± 27 Ma (MSWD = 1.5), which we consider the crystallization age, with a weighted mean $^{207}Pb/^{206}Pb$ age of 1803 ± 6 (8 grains, MSWD = 3.2). Thermal resetting is indicated by six zircons that provide concordant dates between 1600 and 1700 Ma, with one measurement at ca. 1550 Ma (Fig. 7).

KAC74-71 is a medium-grained granodiorite from a septum in the central part of the Kunene Complex. Ten analyses (on 10 zircon grains) plot on a concordia and yield a date of 1947 ± 4 Ma (MSWD = 1.5), with an identical weighted mean $^{207}Pb/^{206}Pb$ age (1947 ± 4 Ma, 10 grains, MSWD = 0.8). We interpret this age as the crystallization age of the granodiorite. One zircon grain provides a concordant date of 2467 ± 14 Ma, which represents the oldest age obtained from the basement rocks so far in the literature.

KAC254-250 is a lit-par-lit injection of a dm-scale granodiorite sill in the migmatitic basement from the southwestern Angolan Kunene Complex. Fourteen analyses (on 13 zircons) plot on a discordia and yield a date of 1800 ± 5 Ma (MSWD = 0.7), which we interpret as the crystallization age, with a weighted mean $^{207}Pb/^{206}Pb$ age of 1794 ± 3 Ma (13 grains, MSWD = 0.7).

Sample KSAT35-22 is a medium-grained heavily altered anorthosite from the Caongoquepia mafic intrusion (Angola). It consists mainly of euhedral to subhedral laths of sericitized plagioclase and interstitial chloritized pyroxene, and contains a few euhedral to subhedral zircons that are < 200 µm in size. Two zircon grains have been dated in thin section and provide a concordant date of 1780 ± 11 Ma (MSWD = 1.9), which we interpret as the crystallization age, with a weighted mean $^{207}Pb/^{206}Pb$ age of 1804 ± 9 Ma (5 grains, MSWD = 6.7).

4.4. Hf isotopes

Table 3 shows a summary of the average εHf compositions of zircon grains from 14 Red Granite Suite samples and six basement samples (full dataset in Table 2SM, supplementary material). The four xenocrysts in KAC274 (ages at ca. 2050 Ma) were also analyzed.

Initial epsilon Hf values calculated at their crystallization age for the Red Granite Suite are bracketed between −8.3 and + 0.2 (as sample averages, Fig. 1, Fig. 8, and Table 3). The highest $\varepsilon Hf_{(t)}$ value (+1.6) was measured in KAC31-35, while the lowest value (–11.3) was measured in KAC186-188. The 11 Red Granite Suite samples in the southern sector of the Kunene Complex have average $\varepsilon Hf_{(t)}$ values that are constrained between −6.1 and + 0.2, whereas the 2 samples in the northernmost part of the Kunene Complex have average $\varepsilon Hf_{(t)}$ values of + 0.9 (KAC269-269) and −8.3 (KAC186-188). No correlation seems to exist between crystallization age and εHf, as the two samples older than 1410 Ma (KAC260-254 and KAC274) have average $\varepsilon Hf_{(t)}$ at ca. −4 and are within the range of the rest of the Red Granite Suite rocks.

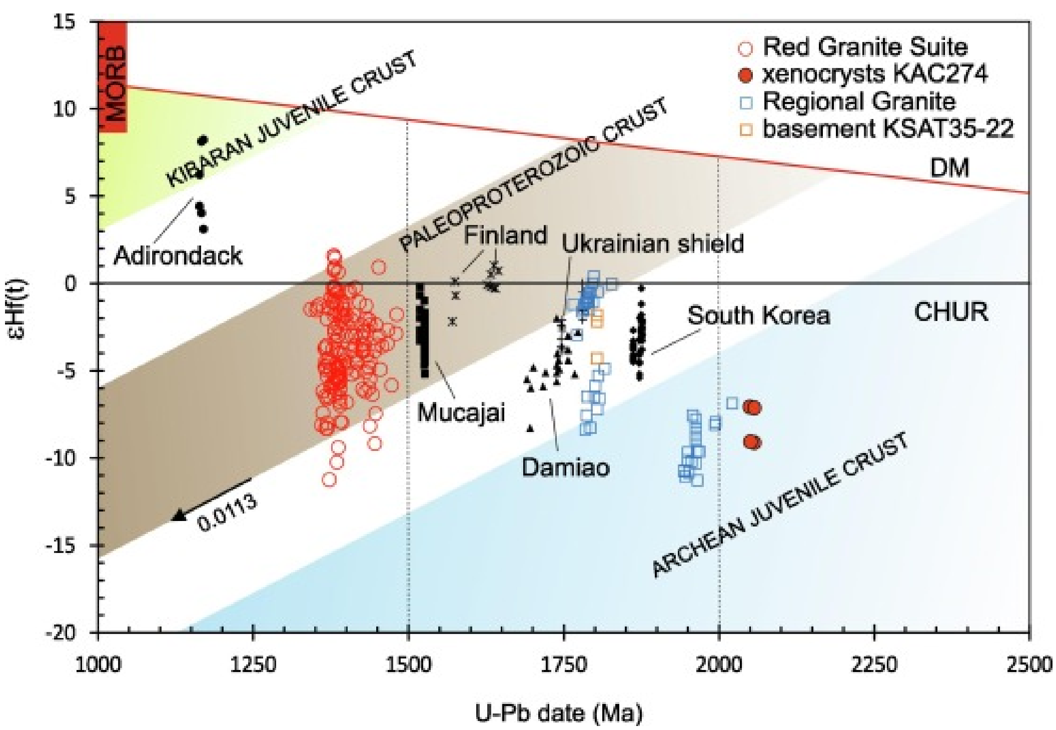

Fig. 8. $\varepsilon Hf_{(t)}$ vs. U–Pb age diagram showing the results of analyzed zircon grains from the Red Granite rocks (red circles) and 4 granitoid rocks plus an anorthositic rock from the basement (blue and orange squares, see text). The crust evolutionary trends of source components from hypothetical DM melts are shown in different colors. A compilation of Hf isotope compositions of zircons from AMCG suites is also plotted. Star = Southern Finland (Heinonen et al., 2010); plus = Ukrainian shield (Shumlyanskyy et al., 2017); circle = Adirondack, North America (McLelland et al., 2004); square = Mucajaí complex, northern Amazonian craton (Heinonen et al., 2012); black triangle = Damiao complex, North China (Zhao et al., 2009); diamond = Sancheong and Hadong, South Korea (Lee et al., 2017). Arrow at bottom left marks the evolution of average continental crust with $^{176}Lu/^{177}Hf$ = 0.0113 (Rudnick and Gao, 2003). For details and references for depleted mantle (DM) evolution and chondritic uniform reservoir (CHUR) parameters, see Gerdes and Zeh (2006).

The basement granitoids from the southern Kunene Complex (dated at 1800–1780 Ma) have slightly unradiogenic $\varepsilon Hf_{(t)}$, with average values of −1.2 (KAC27-31) and −0.6 (KAC254-

Table 3. Summary of average εHf(t) results for the Kunene granitoids and basement host rocks. U-Pb zircon dates from [a] Lehmann et al. (2020) and [b] this work.

Sample	Empty Cell	Empty Cell	**Rock**	**$\varepsilon Hf_{(t)}$**	**± 2σ**	**# zircon grains**	**TDM (Ga)**	**U-Pb Age**	**Age type**
Red Granite Suite	**Long E (dec deg)**	**Lat S (dec deg)**							
KAC23-28A	13.485900	16.781190	Megacrystic augen gneiss	−5.2	2.1	8	2.1	1391 ± 9 [a]	weighted mean
KAC31-35	13.469986	16.941510	Undeformed medium-grained granite	0.2	2.3	12	1.8	1380 ± 5 [a]	upper intercept
KAC34-37A	13.441027	16.681810	Undeformed megacrystic granite	−5.4	1.6	11	2.1	1393 ± 7 [a]	upper intercept
KAC35-38A	13.449689	16.593061	Fine-grained granite gneiss	−5.7	0.8	11	2.2	1387 ± 8 [a]	upper intercept
KAC35-38B*	13.449689	16.593061	Microgranite in KAC35-38A	−6.1	2.7	11	2.2	1391 ± 14 [a]	weighted mean
KAC43-43	13.678043	16.550546	Granite augen gneiss	−3.3	1.9	11	2.1	1442 ± 8 [a]	weighted mean
KAC43-44	13.678043	16.550546	Fine-grained microgranite dyke	−4.6	1.0	12	2.1	1372 ± 5 [a]	upper intercept
KAC61-58	13.923343	16.499553	Undeformed medium-grained granite	−2.9	1.3	11	2.0	1386 ± 5[b]	concordia
KAC186-188	14.081797	15.414246	Medium- to fine-grained granite gneiss	−8.3	3.5	12	2.3	1370 ± 9[b]	concordia
KAC260-254	13.708975	15.923305	Undeformed megacrystic qz monzonite	−3.7	1.4	12	2.1	1414 ± 4[b]	concordia
KAC269-269	13.889764	15.595566	Granite gneiss	−0.9	1.7	9	1.9	1374 ± 10[b]	upper intercept
KAC274	13.635403	17.086877	Undeformed fine-grained granite	−4.0	3.1	11	2.1	1441 ± 3[b]	concordia
KAC297	13.538857	17.075111	Undeformed medium-grained granite	−1.2	1.0	12	1.9	1377 ± 4[b]	concordia
KAC301-1	13.362436	16.962940	Granite gneiss	−1.7	2.2	11	1.9	1392 ± 5[b]	concordia
Basement rocks									
KAC27-31	13.463860	16.904320	Granodiorite gneiss	−1.2	1.4	10	2.2	1782 ± 9 [a]	weighted mean
KAC74-71	13.935498	15.837491	Granodiorite	−10.5	1.1	10	2.9	1947 ± 4[b]	concordia
KAC98-92	14.037250	14.945120	Granite	−6.7	2.3	10	2.5	1830 ± 27[b]	upper intercept
KAC119-109	14.425314	14.800068	Granite	−8.3	1.5	10	2.8	1964 ± 3[b]	concordia
KAC254-250	13.452443	16.874024	Granodiorite sill	−0.6	1.2	9	2.2	1800 ± 5[b]	upper intercept
KSAT35-22	13.558591	15.784633	Anorthosite	−2.8	2.7	3	2.3	1780 ± 11[b]	concordia

TDM Two-stage model age in billion years using the measured $^{176}Lu/^{177}Hf$ of each spot (first stage = age of zircon), a value of 0.0113 for the average continental crust (second stage), and an average;

MORB (DM) $^{176}Lu/^{177}Hf$ and $^{176}Hf/^{177}Hf$ of 0.0384 and 0.28314, respectively. * the attribution of KAC35-38B (microgranite in KAC35-38A) as part of the Red Granite Suite is unclear.

Geographic coordinate systems (GCS) in decimal degrees.

250). More unradiogenic values were obtained for the oldest (1970–1950 Ma) basement rocks sampled to the north-northwest of the Kunene area, with average $\varepsilon Hf_{(t)}$ values of −8.3 (KAC119-110) and −10.5 (KAC74-71). Sample KAC98-92 (ca. 1800 Ma) has an average $\varepsilon Hf_{(t)}$ of −6.7. The four xenocrysts (ca. 2050 Ma) in sample KAC274 have an $\varepsilon Hf_{(t)}$ of −7.1 to −9.1.

Sample KSAT35-22 from the Caongoquepia mafic intrusion (1780 Ma) has an $\varepsilon Hf_{(t)}$ of −2.8, which overlaps with the initial Hf values of the coeval granitoids in the basement (Fig. 8).

5. Discussion

5.1. Geochemical affinity: A-type, I-type granitoids and high-silica rocks

Most of the Red Granite Suite samples from the Kunene AMCG Complex that were investigated in this study are characterized by high FeO/FeO + MgO, high (Na_2O + K_2O)/Al_2O_3, and relatively low Ca and Al contents. They generally show an A-type character (after Loiselle and Wones, 1979), with the exception of samples KAC43-45, KAC208-205 and KAC221-219. Such an affinity is emphasized by the discrimination diagrams of Whalen et al. (1987) in Fig. 9a, b, and is also supported by other features that are distinctive of A-type granites, such as the alkali-calcic to alkali character (Frost et al., 2001), relatively high Ti/Mg, K_2O/Na_2O and Ga/Al, enrichment in LILE and HFSE, as well as negative Sr, P, Ti and Eu anomalies (e.g., Dall'Agnol et al., 1999, and references therein; Jahn et al., 2001, Lenharo et al., 2002, Wu et al., 2002). In the Rb vs. Yb + Nb and Nb vs. Y discrimination diagrams of Pearce et al. (1984), the Red Granite Suite samples plot in the 'within-plate' field (Fig. 9c, d). The Nb vs. Y diagram suggests that there was crustal contamination, as crust has Y/Nb > 1 (Eby, 1992). In the Y-Nb-Ce diagram of Eby (1992), most of our Red Granite Suite samples plot in the A2 field, and this is compatible with the magmas being derived from continental (or underplated) crust related to subduction or continent–continent collision (Fig. 2 in supplementary material).

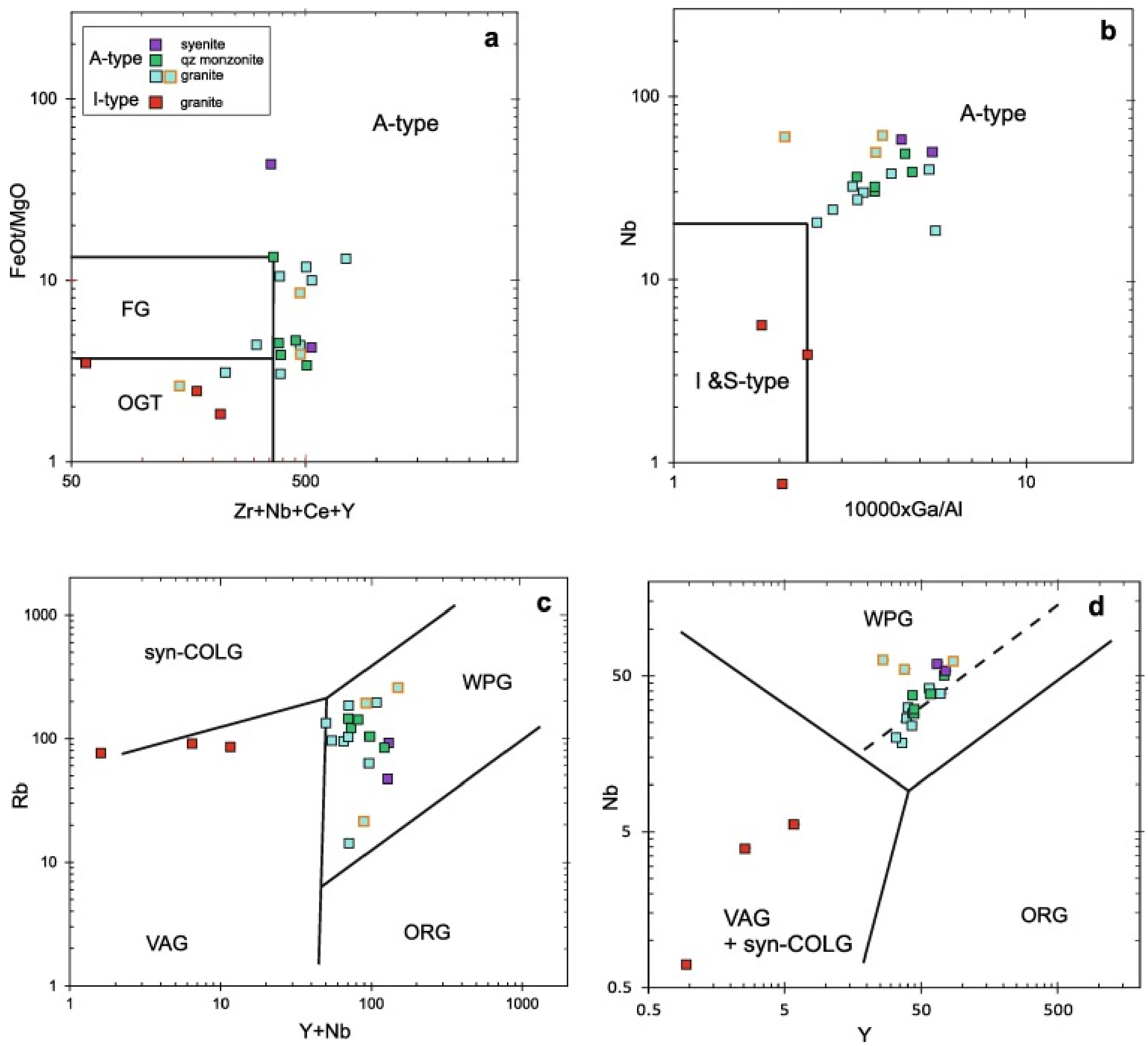

Fig. 9. Tectonic discrimination diagrams for the Red Granite Suite rocks. a) FeO/MgO vs. Zr + Nb + Ce + Y and b) Nb vs. 1000 × Ga/Al (Whalen et al., 1987); FG: fractionated felsic granites; OGT: field for M-, I- and S-type granitoids. c) Rb vs. Y + Nb and d) Nb vs. Y tectonic discrimination diagrams (Pearce et al., 1984); VAG: volcanic arc granites; *syn*-COLG: *syn*-collisional granites; post-COLG: post-collisional granites; ORG: ocean ridge granites; WPG: within plate granites.

The ferroan and metaluminous character of the alkali-calcic and alkalic granitoids is in agreement with the association of these types of rocks with anorthosite and Fe-rich mafic rocks during the Proterozoic, while large ferroan felsic batholiths are rare in the Archean and Phanerozoic (Frost and Frost, 2008, Frost and Frost, 2011, Frost and Frost, 2013). In AMCG suites, felsic and mafic rocks typically coexist, with the felsic rocks ranging from ferrodiorite and monzodiorite, to monzonite, syenite and granite (Frost and Frost, 2011). Our field observations and analytical work indicate that mangerite and charnockite are minor among the Kunene Complex felsic rocks.

The three most evolved (SiO_2 > 76 wt%) leucocratic granites (KAC45-46, KAC269-269, KAC297) with low Ba, Sr, P, Ti, Eu, Zr/Hf, La/Th, Ce/Th, and high Nb, Ta, U and Th, show a characteristic M−type tetrad effect in their REE profiles (Fig. 5e). The REE tetrad pattern was first described by Fidelis and Siekierski (1966) and is common in highly differentiated evolved granites and/or those that are hydrothermally altered (Bau, 1996, Irber, 1999, Lee et al., 1994). The origin of the tetrad effect is still debated, but it is thought that it can be caused by an exotic fluid interacting with the magma (e.g., Monecke et al., 2002). It has been demonstrated that an (external) fluid-magma interaction, resulting in a tetrad effect, can be responsible for a non-CHARAC (CHARAC, charge-and-radius-controlled) behavior in trace elements, including the REE (Bau, 1996). A way to highlight the presence of non-CHARAC behavior is to assess the fractionation between isovalent couples of trace elements such as Y-Ho and Zr-Hf, as these ratios are sensitive to changes in melt composition during magma fractionation (Bau, 1996, Irber, 1999). The tetrad effect could explain these chemical patterns for the three leucogranites assuming chondritic ratios of 24–34 for Y/Ho and 26–46 for Zr/Hf (Bau, 1996) (Fig. 3a in supplementary material), which plot as non-CHARAC (outside of the CHARAC field) with low Zr/Hf and Y/Ho (Fig. 3b in supplementary material).

The petrology and geochemistry of our samples allow us to highlight a minor group of granitoids. Samples KAC43-45, KAC208-205 and KAC221-219 are megacrystic to medium-grained rocks mainly composed of quartz and K-feldspar with negligible plagioclase, ferromagnesian minerals (biotite, amphibole) and oxides. KAC208-205 and KAC221-219 are rocks injected into the basement along the southwestern margin of the Kunene Complex, with the first from a mylonite sheet and the second representing an undeformed vein. The relationship of these two samples with the Kunene Complex is uncertain as no age is available. KAC43-45 is a foliated porphyritic gneiss from a domain of Red Granite Suite located within the Kunene anorthosites. The rock has a positive Eu anomaly (Fig. 5f) that is likely related to high temperature water–rock interaction (Nakada et al., 2017). The three rocks are alkali-calcic, magnesian, weakly peraluminous, depleted in REE, Nb, Ta, Zr, Y, Ga, Ti, P, enriched in Ca (Fig. 3c, d, Fig. 4, Fig. 5f), and they show an affinity to I-S-type granites (Fig. 9b) and collisional settings (Fig. 9c, d), which indicates that these granites are derived from a different source. The negative correlation between SiO_2 and P_2O_5 is indicative of apatite saturation, and the lack of Al-rich minerals suggests an I-type character (e.g., Chappell, 1999). The I-type and magnesian character, and the marked Nb-Ta and Ti negative anomalies, are comparable to subduction-related granitoids (e.g., Frost et al., 2001). The low Y and Sr concentrations, and the concave-upward pattern from middle to heavy REE are consistent with hornblende and plagioclase fractionation (Romick et al., 1992), or could indicate partial melting of a mafic crust with plagioclase and hornblende as residual phases (Hastie et al., 2010, Jiang et al., 2018).

5.2. Spatial-temporal extent of the Red Granite Suite

Based on the geochemical and geochronological evidence discussed here, we infer that the Mesoproterozoic granites within and around the Zebra Mountains in Namibia are part of the Red Granite Suite. The ages determined in this study, and in recent studies on the granitoids of the Kunene Complex, show that the emplacement of the Red Granite Suite is bracketed between 1450 and 1360 Ma (de Carvalho and Alves, 1990, Morais et al., 1998, Lehmann et al., 2020), thus supporting a coeval to younger relationship with the Kunene anorthosites, which range between 1500 and 1375 Ma (Bybee et al., 2019). The magmatism can be broadly divided into three main stages (1450–1410 Ma, 1400–1380 Ma, 1380–1360 Ma), with approximately half of the dated granitoids being emplaced during the most recent period (Table 2).

According to Bybee et al. (2019), three age clusters have been proposed from north to south for the Kunene anorthosites. The cluster of anorthosite ages in the range 1384–1375 Ma to the north of the NNE-SSW-trending Red Granite Suite belt is in general agreement with the ages in the range 1392–1361 Ma measured on three Red Granite samples from the same belt (KAC186-188, KAC269-269 and the mangerite sample of Mayer et al., 2004, McCourt et al., 2013). Two ages of ca. 1410–1400 Ma for Kunene anorthosites south of Pocolo are in agreement with the age of ca. 1410 Ma measured in the same area for sample KAC260-254 of the Red Granite Suite. A variable temporal distribution is apparent in the southernmost part of the Kunene Complex as indicated by the ages of two anorthosites at ca. 1390 Ma and a leucotroctolite at ca. 1440 Ma. This is in agreement with the wide range of ages obtained for the Red Granite Suite rocks in the same region, which span 1440 to 1370 Ma (see Fig. 1 and Table 2). A general time–space correlation between the anorthosites and the Red Granite Suite can therefore be inferred and suggests that both were triggered by the same thermal processes (a summary of published and new radiometric ages for the Kunene Complex and host rocks is presented in Fig. 10).

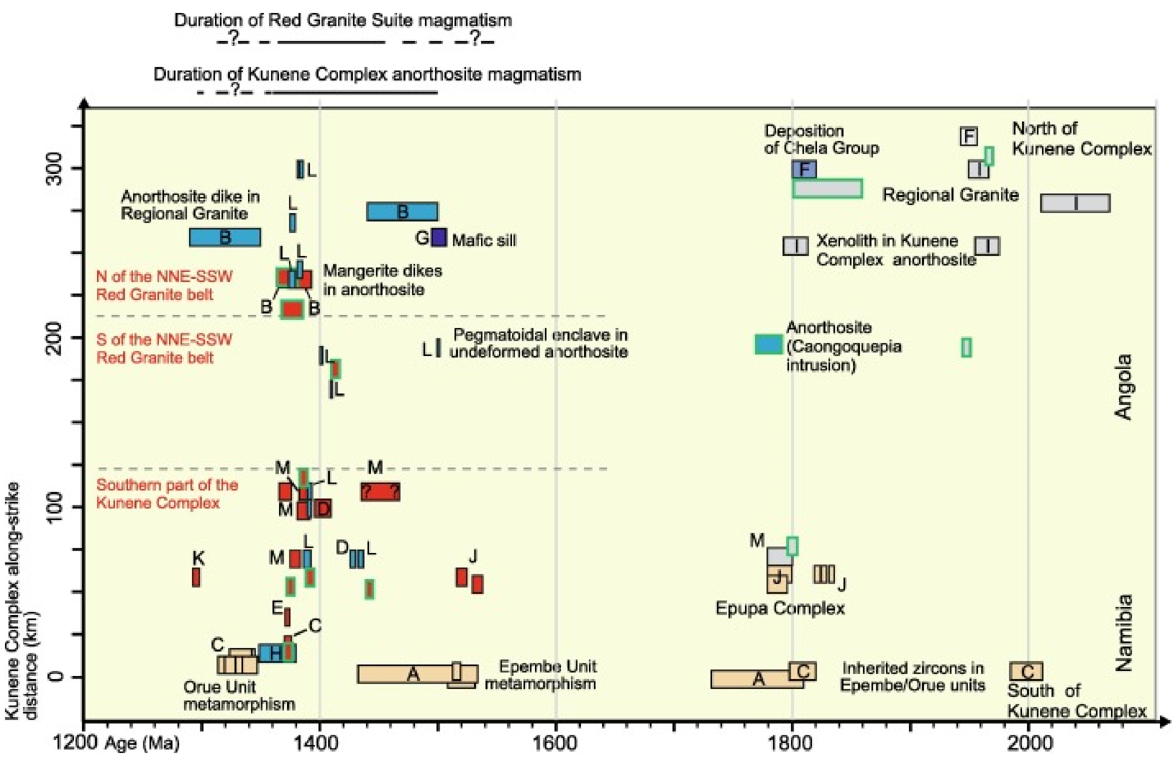

Fig. 10. Summary of the distribution along N-S strike of all the published and new radiometric ages of the Kunene AMCG Complex, and country rocks (modified after Lehmann et al., 2020). The new data are represented with green borders. Data sources: A Seth et al. (2003); B Mayer et al. (2004); C Seth et al. (2005); D Baxe (2007); E Drüppel et al. (2007); F Pereira et al. (2011); G Ernst et al. (2013); H Maier et al. (2013); I McCourt et al. (2013); J Kröner et al. (2015); K Kröner and Rojas-Agramonte (2017); L Bybee et al. (2019); M Lehmann et al. (2020). Colors as in Fig. 1.

The affiliation of the Red Granite Suite to the dated granitoids sampled 60 to 100 km to the south of the Kunene River and along the Kunene River to the west and east of the Zebra Mountains (Kröner et al., 2015, Kröner and Rojas-Agramonte, 2017) is not straightforward. Granitoids located 60 to 100 km to the south of the Kunene River (Na41, Na71, dated ca. 1250–1220 Ma, and Na77, Na87, Na96 ca. 1440–1350 Ma, in Kröner and Rojas-Agramonte (2017)) show some chemical differences compared to our samples: besides being in part substantially younger than the Red Granite Suite (<1250 Ma), these granitoids are magnesian, relatively low in Ga, Nb, Zr, Y and alkali content, and are compatible with I-S types (Whalen et al., 1987). In contrast, the granitoids collected along the Kunene River to the west and east of the Zebra Mountains (1375–1175 Ma) show more chemical similarities with the Red Granite Suite. However, there is a gap in the emplacement age of these granites between 1350 and 1250 Ma and so only the older granites may be part of the Red Granite Suite.

5.3. Paleoproterozoic basement

The four Regional Granite samples are dated between 1965 and 1800 Ma and the anorthositic basement rock from the Caongoquepia intrusion has an age of 1780 Ma. These ages are in agreement with previously reported ages for the basement of the Kunene Complex in northern Namibia (e.g., Kröner et al., 2010, 2015) and SW Angola (Jelsma et al., 2018, Lehmann et al., 2020). The two xenocrysts in KAC274 that were dated at 1790–1770 Ma are also in agreement (Table 1SM in supplementary material). The xenocrystic ages of ca. 2050 Ma in KAC274 are similar to the ages of detrital zircons (ca. 2035 Ma) in a quartzo-feldspathic paragneiss along the Kunene River to the west (Kröner et al., 2015). Similar ages have been obtained in the Regional Granite of the Humpata Plateau (250 km to the north), where a U-Pb zircon age and a less well constrained Rb-Sr age have been measured (Torquato et al., 1979, McCourt et al., 2013).

Paleoproterozoic magmatism has been recognized in NW Namibia in a crustal block extending into Kaokoland (Seth et al., 1999, Kröner et al., 2010, McCourt et al., 2013) and further to the south in the Kamanjab and Abbabis inliers of the northern Damara Belt (Tack et al., 2002, Miller, 2008, Jelsma et al., 2018). The ages of ca. 1965 Ma for the northernmost basement, and 1800–1780 Ma for the southwestern basement of the Kunene Complex in Angola, agree with the known different magmatic provinces in SW Angola and NW Namibia (Jelsma et al., 2018): the Eburnean Event (2.0–1.96 Ga) and Epupa Event (1.80–1.77 Ga). In addition, the new ages of 1800–1780 Ma confirm the extension of the northern Namibian Epupa Event to SW Angola. These tectonomagmatic domains have been interpreted as part of a 2.05–1.76 Ga system of continental arcs (e.g., Kröner et al., 2010, Jelsma et al., 2018), which are thought to extend further to the east in the Tsumkwe inlier of northeastern Namibia (dated at ca. 2020 Ma, in Hoal et al., 2000), in the Quangwadum region of northwestern Botswana (dated at ca. 2050 Ma, in Singletary et al., 2003), and in the Lufubu Metamorphic Complex of NW Zambia (dated at 1980–1870 Ma, Rainaud et al., 2005, Jelsma et al., 2018).

5.4. Petrogenetic constraints using Hf isotopes in zircon

The Hf isotope compositions recorded in the Red Granite Suite samples are comparable to those measured in other AMCG suites worldwide (Table3, Fig. 8), but the variability in initial εHf values (from −11.3 to + 1.6) is higher than in any other AMCG suite (e.g., Shumlyanskyy et al., 2017, Fig. 8; Table 2SM in supplementary material). Projection of the $\varepsilon Hf_{(t)}$ composition of the Paleoproterozoic basement rocks, according to an average continental crust $^{176}Lu/^{177}Hf$ of 0.0113 (Rudnick and Gao, 2003, Fig. 8), results in highly unradiogenic Hf (from ca. −20 to ca. −8 $\varepsilon Hf_{(t)}$), suggesting mixing between an unradiogenic crustal component and a radiogenic juvenile mantle-derived component. The range in εHf (+0.4 to −11.3) in the five Regional Granite samples (Fig. 8 and Table 3: Table 2SM in supplementary material) suggests that the basement rocks likely represent the crustal component, but an unradiogenic Archean component cannot be excluded. The four xenocrysts (ca. 2055 Ma) in sample KAC274 in the southern part of the Kunene Complex overlap with the $\varepsilon Hf_{(t)}$ composition of the oldest basement rocks in the northern Kunene Complex (sample KAC119-109, Table 3, Table 2SM, supplementary material), and suggest the presence of a relatively uniform unradiogenic basement component at around 2.0 Ga throughout the complex. As to the radiogenic juvenile component, a mantle-derived magma (i.e., parent magmas to the Kunene anorthosites), and/or a component derived from the lower crust, and which was melted during the emplacement of the Kunene anorthosites, can be proposed. The zircons in the Caongoquepia intrusion (KSAT35-22), potentially a source of information on a Paleoproterozoic mantle component, show $\varepsilon Hf_{(t)}$ values comparable with thoseof the Paleoproterozoic granitoids (Table 3, Fig. 8). Such overlap in Hf isotopes between mantle and crustal sources is not surprising (e.g., Bickford et al., 2010), but prevents a better characterization of the mantle component.

Separate (mantle-crustal) sources for the A and MCG (e.g., Bybee et al., 2014, Emslie et al., 1994, Shumlyanskyy et al., 2012, Lee et al., 2017), or derivation from a common lower crust melt (e.g., Duchesne et al., 1999, Longhi et al., 1999, Vander Auwera et al., 2011) have been inferred to explain the nature of AMCG components. According to a consolidated model, mantle-derived magmas ponded at Moho depths of 30–40 km undergo gravitational settling of mafic silicates and separation and flotation of plagioclase-rich mushes that ascend through the crust. The coeval anatexis of crustal material caused by heat released from the ponded mafic magma would generate the MCG rocks (Emslie, 1985, Longhi and Ashwal, 1985, McLelland et al., 2010, Scoates, 2000). Derivation from pure crustal melts is unlikely (Bonin, 2007, Frost and Frost, 1997), and isotopic studies support mixing of a mantle component with older and enriched crustal material (e.g., Anderson et al., 2003, Bonin, 2007, Fraga, 2009, Scoates and Chamberlain, 2003, Shumlyanskyy et al., 2017).

O-Sr-Nd-Os isotopic evidence shows that the Namibian Kunene anorthosites originated from the upper mantle and were contaminated by the crust (Drüppel et al., 2007, Gleißner et al., 2010, Gleißner et al., 2011, Gleißner et al., 2012). However, O isotopes indicate geochemically different sources for the anorthosites and the granitoids, suggesting a mantle origin for the anorthosites, and then anatexis of lower crust, with or without input of a mantle component, for the origin of the felsic rocks (Drüppel et al., 2007).

Our Hf isotope data for the Red Granite Suite are consistent with a mantle-crust mixing model. We suggest that initial injection of basaltic magma into the crust would have created crustal melts that hybridized with the differentiating and ascending mantle-derived melts, producing intermediate to felsic magma. The latter was a combination of fluid and partially crystallized magma (mush) rising to shallower crustal levels, undergoing further crystallization, mixing, assimilation, storage, homogenization, and replenishment (e.g., Moyen et al., 2021). The variation in type and intensity of these processes, and ultimately the different geochemistry of the crustal material involved, would explain the inter- and intra-sample heterogeneity in Hf isotopes in zircon in the Red Granite Suite (Table 3 and Fig. 8).

5.5. Tectonic setting of the Kunene AMCG Complex

5.5.1. Subduction-collision model

The association of AMCG complexes with extensional environments is still considered valid for many regions such as the Fennoscandian Shield (Lundmark and Corfu, 2008, Rämö and Haapala, 2005), but increasing geochronological and field evidence suggests that AMCG complexes on Earth are compatible with continental margin settings during the terminal stages of an orogenic event (McLelland et al., 2008).

An example is provided by the AMCG magmatism of North America, referred to as a 4,000 km-long continental arc margin active for ca. 800 Ma (e.g., McLelland et al., 2010, and references therein). In support of a continental arc setting for AMCG complexes, it has been observed that geodynamic scenarios including continental rifting, continent–continent collision and waning collisional stages cannot be reconciled with the long time-frame of magmatism, the involvement of large-scale crustal melting, and the preferential arrangement of AMCG suites in linear belts (Ashwal and Bybee, 2017, and referenced therein). Such features are more typical of convergent continental margins, for example in the 1,700 km-long fossil magmatic arc of the Coastal Mountains batholith (Ducea et al., 2015, Gehrels et al., 2009), or in the 1,100 km-long Central American Volcanic Arc of Panama, Costa Rica, and Nicaragua (Buchs et al., 2010, Whattam and Stern, 2015). Convergent continental margins for Proterozoic AMCG magmatism have also been proposed in North China Craton (Lee et al., 2017, and references therein), in the Lofoten–Vesterålen rocks in Norway (Corfu et al., 2004, and references therein), in the Sweconorwegian Orogen (Slagstad et al., 2022), and in the Grenville province of Canada (Corrigan and Hanmer, 1997).

5.5.2. Hot intracontinental orogen model

Linear magmatic belts, prolonged magmatism (in the order of 50 Ma), and crustal contraction are not only the hallmarks of convergent continental margins. These key features are also noted for the Pan-African Araçuaí-Ribeira-Congo and Dom Feliciano-Kaoko-Gariep orogenic belts, which have been recently interpreted as hot intracontinental orogens with extensive crustal melting due to thickening (Vauchez et al., 2019, Fossen et al., 2020, Konopásek et al., 2020) and radiogenic heat production from buried sediments (e.g., Cavalcante et al., 2019, and references therein). Although agreement on this model is not unanimous (see Caxito et al., 2022), the authors refuting the subduction-collision model base their argument on the lack of oceanic space and high-P metamorphic rocks, and the very short time span between the end of rifting and the onset of convergence. Their hypothesis admits a negligible contribution of mantle sources, with largely prevailing melting crust (e.g., Gonçalves et al., 2018).

5.5.3. Crustal-mantle contribution in a convergent continental margin setting

The prolonged magmatism of the Kunene Complex could either indicate the existence of a N–S-elongated Andean-type arc situated along the southwestern margin of the Congo Craton or the formation of a hot intracontinental orogen.

Hf isotopes in zircon can help in deciphering the most appropriate between these two models. Zircon in the Red Granite Suite has the largest range in $\varepsilon Hf_{(t)}$ (13.5 epsilon units) compared to other AMCG complexes worldwide (Fig. 8), which can be explained by: i) mixing of (unradiogenic) crustal and (radiogenic) mantle material, which is compatible with a convergent continental margin model, or ii) crustal source heterogeneity, which would be the case in a hot intracontinental orogen.

Crustally-derived granites, with no evidence of addition of mantle material, can show a range in $\varepsilon Hf_{(t)}$ even greater than that observed in the Red Granite Suite (e.g., Villaros et al., 2012, Tang et al., 2014). This happens when the magmatic zircon crystallizes rapidly so that the homogenization of Hf isotopes, due to dissolution of the zircon during mixing and/or diffusion between crustal melts, is only partial (e.g., Davies and Tommasini, 2000, Zeng et al., 2005, Farina and Stevens, 2011). This process requires rapid cooling, and therefore is more likely at shallow depths. In the Red Granite Suite, however, there is little to no evidence of shallow depth emplacement. In the southwestern Kunene in Angola, Lehmann et al. (2020) infer emplacement of the Red Granite Suite and the anorthosites along deep crustal discontinuities. Hayes et al. (2022) constrain granitoid intrusion at mid crustal levels, based on Al-in-hornblende barometry, and Drüppel et al (2001) measured anorthosite crystallization conditions of at 950–985 °C and 7–9 kbar in Namibia. Moreover, in the case of inefficient zircon dissolution in the magma, inherited zircons, as cores or entire grains, will commonly be preserved, and this is not the case for the Red Granite Suite, where xenocrysts have been found only in one sample (KAC274).

Therefore, we infer that the Hf isotopic variability in the Red Granite Suite rocks is due to the contribution of both crustal and mantle material. In accordance with the global evidence of the emplacement of large-scale A-type granites along accretionary margins during the Mesoproterozoic (Anderson and Morrison, 1992, Anderson and Morrison, 2005, Goodge and Vervoort, 2006), we suggest that a convergent continental margin developed in this part of the Congo Craton during the Mesoproterozoic, which was built on the roots of an older magmatic arc that was active during the Paleoproterozoic (Kröner et al., 2015, Jelsma et al., 2018). The inferred absence of large volumes of I-S-type continental arc granites to the west of the Kunene area may be due to large-scale subduction erosion of the advancing margin (e.g., Stern, 2011), which is the mechanism proposed to explain the lack of I-S-type granites in Mesoproterozoic accretionary orogens (Condie, 2013). This would have also been enhanced by contraction in the upper plate, in agreement with *syn*-Kunene deformation that has been documented in southwest Angola (Lehmann et al., 2020). Alternatively, or in conjunction with subduction erosion, I-S-type granites may be concealed under younger supracrustal sequences surrounding the Kunene Complex.

Whether the Kunene MCG magmatism was, at least in part, an expression of an extensional system (back-arc?) or not, is not clear, and we cannot resolve it with our data for the Red Granite Suite. AMCG complexes emplaced in back-arc settings have been proposed in Labrador for the Mesoproterozoic convergent margin of southeastern Laurentia (Condie, 2007, Rivers, 2008, Rivers and Corrigan, 2000) and in the Rogaland Anorthosite Province in the SW Sveconorwegian Orogen (Slagstad et al., 2022). Extension in the Kunene Complex cannot be ruled out before 1400 Ma, a period during which no contraction fabrics have been noted (Lehmann et al., 2020).

An A-type geochemical character is present in the Red Granite Suite for the entire duration of its magmatism, including the contractional period between 1400 and 1380 Ma (Lehmann et al., 2020). This confirms that A-type granites do not only form in extensional settings and an overall extensional tectonic regime may not be applicable to AMCG complexes globally. Prolonged (~90 Myr) A-type granite magmatism in the Kunene AMCG Complex is also difficult to reconcile with anorogenic or post-orogenic settings. A-type granites may also form during late- to post-collisional stages, possibly because of gravitational collapse due to crustal thickening (Bonin, 2007, and references therein), and cases of A-type magmatism associated with orogenic horizontal shortening have been documented (e.g., Milani et al., 2015, Ren et al., 2021, Zhao et al., 2013). A combined geochemical, structural, and geochronological investigation becomes key for constraining the tectonic environment of A-type granites.

6. Conclusions

The Red Granite Suite is part of the Mesoproterozoic Kunene AMCG Complex, forming at least one-third of the exposed rocks of this complex, in Angola and Namibia. The geochemistry of the granitoids did not change substantially during the 90 Myr emplacement window, with alkali-calcic, A-type granites predominant. U-Pb age data from the Red Granite Suite show that the peak of A-type granite magmatism is bracketed between 1380 and 1360 Ma, but some of our ages extend magmatism to 1450 Ma. This corroborates previous findings that showed that Kunene anorthosite magmatism lasted > 100 Myr. Three age clusters were recognized from north to south in the Kunene anorthosites in Angola and they roughly correlate with the age distribution of the Red Granite Suite in the northern, central, and southern sectors. This suggests that anorthosite magmatism played an important role in triggering crustal anatexis and the petrogenesis of the MCG component. The A-type signature and Hf isotope chemistry of the Red Granite Suite did not change significantly during protracted magmatism, including during the documented E–W contraction between 1400 and 1380 Ma, thus challenging the notion that A-types granitoids are the exclusive products of magmatism in extensional environments. Hf isotopic data of zircons from the Red Granite Suite and Paleoproterozoic basement (including a mafic intrusion) are consistent with the derivation of magmas from mixing of recycled Paleoproterozoic (or Archean) crust with a juvenile mantle component. Parent basalts to the Kunene anorthosites that ponded at the Moho led to melting of the Paleoproterozoic crust and the protracted emplacement of dominantly A-type granitoids. The long-time span for Kunene AMCG Complex magmatism, and the requirement for both mantle-derived and extensive crustal magmatism are compatible with a convergent continental margin and reinforce the view that Proterozoic massif-type anorthosites and related granitoids can be generated in arc environments undergoing regional shortening.

CRediT authorship contribution statement

Lorenzo Milani: Conceptualization, Writing – original draft, Methodology, Investigation, Data curation. **Jérémie Lehmann:** Conceptualization, Writing – review & editing, Supervision. **Grant M. Bybee:** Conceptualization, Writing – review & editing. **Ben Hayes:** Conceptualization, Writing – review & editing. **Trishya M. Owen-Smith:** Conceptualization, Writing – review & editing. **Lize Oosthuizen:** Software, Visualization, Data curation. **Pieter W.J. Delport:** Methodology, Resources, Validation. **Henriette Ueckermann:** Methodology, Resources.

Declaration of Competing Interest

The authors declare that they have no known competing financial interests or personal relationships that could have appeared to influence the work reported in this paper.

Acknowledgements

The authors are grateful to Stuart John Buchanan and Jorinda van Coller for collecting part of the U-Pb dates during their postgraduate studies at the University of Pretoria. Thanks go to Jeanette Dykstra for her assistance during the processing of the XRF data. James Scoates and an anonymous reviewer were essential to the production of the paper and are warmly thanked for their contribution. The analytical work was funded by an RDP (Research Development

Program) grant awarded to LM at the University of Pretoria. Martin le Roux is thanked for guiding the authors in the field in 2015 and 2016. This work was partly supported by the DSI-NRF Centre of Excellence for Integrated Mineral and Energy Resource Analysis (DSI-NRF CIMERA). The LA-MC-ICPMS equipment at UJ has been funded by NRF-NEP grant #93208, and its operation is supported by DST-NRF CIMERA.

References

Alkmim, F.F., Marshak, S., Pedrosa-Soares, A.C., Peres, G.G., Cruz, S.C.P., Whittington, A., 2006. Kinematic evolution of the Araçuaí-West Congo orogen in Brazil and Africa: nutcracker tectonics during the Neoproterozoic assembly of Gondwana. Precambr. Res. 149 (1–2), 43–64.

Anderson, I.C., Frost, C.D., Frost, B.R., 2003. Petrogenesis of the Red Mountain pluton, Laramie anorthosite complex, Wyoming: implications for the origin of A-type granite. Precambr. Res. 124, 243–267.

Anderson, J.L., Morrison, J., 1992. The role of anorogenic granites in the Proterozoic crustal development of North America. In: Condie, K.C. (Ed.), Proterozoic Crustal Evolution. Elsevier Science Publishers, Amsterdam, pp. 263–299.

Anderson, J.L., Morrison, J., 2005. Ilmenite, magnetite, and peraluminous Mesoproterozoic anorogenic granites of Laurentia and Baltica. Lithos 80, 45–60.

Ashwal, L.D., 1993. Anorthosites. Springer-Verlag, Berlin, Germany, p. 422.

Ashwal, L.D., 2010. The temporality of anorthosite. The Canadian Mineralogist 48 (4), 711–728.

Ashwal, L.D., Bybee, G.M., 2017. Crustal evolution and the temporality of anorthosites. Earth Sci. Rev. 173, 307–330.

Ashwal, L.D., Twist, D., 1994. The Kunene complex, Angola/Namibia: a composite massif-type anorthosite complex. Geology Magazine 131, 579–591.

Bau, M., 1996. Controls on the fractionation of isovalent trace elements in magmatic and aqueous systems: evidence from Y/ Ho, Zr/Hf, and lanthanide tetrad effect. Contrib. Miner. Petrol. 123, 323–333.

Baxe, O.S.S., 2007. Geocronologia de complexos máfico-ultramáficos: exemplo da série superior do complexo de Niquelândia, Brasil, e do complexo Kunene, Angola. M.Sc. Dissertation (unpublished), 1–77.

Bettencourt, J.S., Tosdal, R.M., Leite, J.W.B., Payolla, B.L., 1999. Mesoproterozoic rapakivi granites of the Rondônia Tin Province, southwestern border of the Amazonian craton, Brazil: I. reconnaissance U-Pb geochronology and regional implications. Precambr. Res. 95, 41–67.

Bickford, M.E., McLelland, J.M., Mueller, P.A., Kamenov, G.D., Neadle, M., 2010. Hafnium isotopic compositions of zircon from Adirondack AMCG suites: Implications for the petrogenesis of anorthosites, gabbros, and granitic members of the suites. Can. Mineral. 48, 751–761.

Blanchard, J.A., Ernst, R.E., Samson, C., 2017. Gravity and magnetic modelling of layered mafic–ultramafic intrusions in large igneous province plume centre regions: case studies from the 1.27 Ga Mackenzie, 1.38 Ga Kunene-Kibaran, 0.06 Ga Deccan, and 0.13–0.08 Ga High Arctic events. Can. J. Earth Sci. 54, 290–310.

Bonin, B., 2007. A-type granites and related rocks: evolution of a concept, problems and prospects. Lithos 97, 1–29.

Boynton, W.V., 1985. Cosmochemistry of the rare earth elements: meteorite studies. In: Henderson, P. (Ed.), Rare Earth Element Geochemistry. Developments in Geochemistry 2. Elsevier, Amsterdam, pp. 115–152.

Brandt, S., Klemd, R., 2008. Upper-amphibolite facies partial melting of paragneisses from the Epupa Complex, NW Namibia, and relations to Mesoproterozoic anorthosite magmatism. J. Metamorph. Geol. 26, 871–893.

Brandt, S., Klemd, R., Okrusch, M., 2003. Ultrahigh-temperature metamorphism and multistage evolution of garnet–orthopyroxene granulites from the Proterozoic Epupa Complex, NW Namibia. J. Petrol. 44, 1121–1144.

Brandt, S., Klemd, R., Xie, H., Bobek, P., 2021. Unravelling the P-T-t history of three high-grade metamorphic events in the Epupa Complex, NW Namibia: implications for the Paleoproterozoic to Mesopreterozoic evolution of the Congo Craton. Am. J. Sci. 321, 235–296.

Brandt, S., Will, T.M., Klemd, R., 2007. Magmatic loading in the Proterozoic Epupa Complex, NW Namibia, as evidenced by ultrahigh-temperature sapphirine-bearing orthopyroxene–sillimanite–quartz granulites. Precambr. Res. 153 (3–4), 143–178.

Buchs, D.M., Arculus, R.J., Baumgartner, P.O., BaumgartnerMora, C., Ulianov, A., 2010. Late Cretaceous arc development on the SW margin of the Caribbean Plate: Insights from the Golfito, Costa Rica, and Azuero, Panama, complexes. Geochem. Geophys. Geosyst. 11 https://doi.org/10.1029/2009GC002901.

Bybee, G.M., Ashwal, L.D., Shirey, S.B., Horan, M., Mock, T., Andersen, T.B., 2014. Pyroxene megacrysts in Proterozoic anorthosites: Implications for tectonic setting, magma source and magmatic processes at the Moho. Earth Planet. Sci. Lett. 389, 74–85.

Bybee, G.M., Hayes, B., Owen-Smith, T.M., Lehmann, J., Brower, A.M., Ashwal, L.D., Hill, C.M., Corfu, F., Manga, M., 2019. Proterozoic massif-type anorthosites as the archetypes of long-lived magmatic systems: new evidence from the Kunene Anorthosite Complex (Angola). Precambr. Res. 332 (15), 105393.

Caxito, F.A., Hartmann, L.A., Heilbron, M., Pedrosa-Soares, A.C., Bruno, H., Basei, M.A. S., Chemale, F., 2022. Multi-proxy evidence for subduction of the Neoproterozoic Adamastor Ocean and Wilson cycle tectonics in the South Atlantic Brasiliano Orogenic System of Western Gondwana. Precambr. Res. 376, 106678.

Cavalcante, C., Fossen, H., Paes de Almeida, R., Hollanda, M.E.B.M., Egydio-Silva, M., 2019. Reviewing the puzzling intracontinental termination of the Araçuaí-West Congo orogenic belt and its implications for orogenic development. Precambr. Res. 322, 85–98.

Chappell, B.W., 1999. Aluminium saturation in I- and S-type granites and the characterization of fractionated haplogranites. Lithos 46, 535–551.

Chatterjee, N., Crowley, J.L., Ghose, N.C., 2008a. Geochronology of the 1.55 Ga Bengal anorthosite and Grenvillian metamorphism in the Chotanagpur gneissic complex, eastern India. Precambr. Res. 161, 303–316.

Chatterjee, N., Crowley, J.L., Mukherjee, A., Das, S., 2008b. Geochronology of the 983-Ma Chilka Lake anorthosite, Eastern Ghats Belt, India: implications for pre-Gondwana tectonics. J. Geol. 116, 105–118.

Condie, K.C., 2007. Accretionary orogens in space and time, in Hatcher, R.D., Jr., Carlson, M.P., McBride, J.H., and Martínez Catalán, J.R., eds., 4-D Framework of Continental Crust: Geological Society of America Memoir 200, 13 pp.

Condie, K.C., 2013. Preservation and recycling of crust during accretionary and collisional phases of Proterozoic orogens: a bumpy Road from Nuna to Rodinia. Geosciences 3, 240–261.

Corfu, F., 2004. U-Pb Age, setting and tectonic significance of the anorthosite–mangerite–charnockite–granite suite, Lofoten-Vesterålen, Norway. J. Petrol. 45, 1799–1819.

Corrigan, D., Hanmer, S., 1997. Anorthosites and related granitoids in the Grenville orogen: a product of convective thinning of the lithosphere? Geology 25, 61–64.

Dall'Agnol, R., Scaillet, B., Pichavant, M., 1999. An experimental study of a lower Proterozoic A-type granite from the Eastern Amazonian craton, Brazil. J. Petrol. 40, 1673–1698.

Davies, G.R., Tommasini, S., 2000. Isotopic disequilibrium during rapid crustal anatexis: implications for petrogenetic studies of magmatic processes. Chem. Geol. 162, 169–191.

de Carvalho, H., Alves, P., 1990. Gabbro-anorthosite complex of SW-Angola/NW Namibia. instituto de Investigacão Cientifica Tropical. Serie Ciencias da Terra. Lisboa Commun. 2, 1–66.

de Carvalho, H., Alves, P., 1993. The Precambrian of SW Angola and NW Namibia. Commun. Instituto de Investigação Cientifica Tropical série de ciencias da terre 4, 1–38.

de Carvalho, H., Crasto, J., Silva, Z.C., Vialette, Y., 1987. The Kibarian cycle in Angola: a discussion. Geol. J. 22, 85–102.

de Waard, D., 1968. The anorthosite problem: the problem of the anorthosite-charnockite suite of rocks. In: Isachsen, Y.W. (Ed.), Origin of anorthosite and related rocks, Memoir. 18. New York State Museum and Science Service, pp. 71–91.

Dobmeier, C., 2006. Emplacement of Proterozoic massif-type anorthosite during regional shortening: evidence from the Bolangir anorthosite complex (Eastern Ghats Province, India). Int. J. Earth Sci. 95, 543–555.

Drüppel, K., Littmann, S., Romer, R.L., Okrusch, M., 2007. Petrology and isotope geochemistry of the Mesoproterozoic anorthosite and related rocks of the Kunene Intrusive Complex, NW Namibia. Precambr. Res. 156, 1–31.

Drüppel, K., von Seckendorff, V., Okrusch, M., 2001. Subsolidus reaction textures in the anorthositic rocks of the southern part of the Kunene Intrusive Complex, NW Namibia. Eur. J. Mineral. 13, 289–309.

Ducea, M.N., Saleeby, J., Bergantz, G., 2015. The Architecture, chemistry, and evolution of continental magmatic Arcs. Annu. Rev. Earth Planet. Sci. 43, 231–299.

Duchesne, J.C., Liégeois, J.P., Vander Auwera, J., Longhi, J., 1999. The crustal tongue melting model and the origin of massive anorthosites. Terra Nova 11, 100–105.

Eby, G.N., 1992. Chemical subdivision of the A-type granitoids: petrogenetic and tectonic implications. Geology 20, 641–644.

Emslie, R.F., 1975. Pyroxene megacrysts from anorthositic rocks: new clues to the sources and evolution of parent magmas. Can. Mineral. 13, 138–145.

Emslie, R.F., 1978. Anorthosite massifs, Rapakivi granites, and late Proterozoic rifting of North America. Precambr. Res. 7, 61–98.

Emslie, R.F., 1985. Proterozoic anorthosite massifs. In: Tobi, A.C., Touret, J.L.R. (Eds.), The Deep Proterozoic Crust in the North Atlantic Provinces, NATO ASI Series, Col. 158. D. Reidel, Amsterdam, pp. 39–60.

Emslie, R.F., Hamilton, M., Theriault, R., 1994. Petrogenesis of a mid-Proterozoic anorthosite-mangerite-charnockite-granite (AMCG) complex: isotopic and chemical evidence from the Nain Plutonic Suite. J. Geol. 102, 539–558.

Ernst, R.E., Pereira, E., Hamilton, M.A., Pisarevsky, S.A., Rodriques, J., Tassinari, C.C.G., Teixeira, W., Van-Dunem, V., 2013. Mesoproterozoic intraplate magmatic ‘barcode’ record of the Angola portion of the Congo craton: newly dated magmatic events at 1500 and 1110 Ma and implications for Nuna (Columbia) supercontinent reconstructions. Precambr. Res. 230, 103–118.

Farina, F., Stevens, G., 2011. Source controlled 87Sr/86Sr isotope variability in granitic magmas: the inevitable consequence of mineral-scale isotopic disequilibrium in the protolith. Lithos 122, 189–200.

Ferguson, J., McIver, J.R., Danchlin, R.V., 1975. Fenitisation associated with the alkaline-carbonatite complex of Epembe, South West Africa. Trans. Geol. Soc. South Africa 78, 111–121.

Fidelis, I., Siekierski, S., 1966. The regularities in stability constants of some Rare Earth complexes. J. Inorganic Nuclear Chem. 28, 185–188.

Fossen, H., Cavalcante, C., Konopásek, J., Meira, V.T., de Almeida, R.P., Hollanda, M.H.B., Trompette, R., 2020. A critical discussion of the subduction-collision model for the Neoproterozoic Araçuaí-West Congo orogeny. Precambr. Res. 343, 105715.

Fraga, L.M.B., Dall'Agnol, R., Costa, J.B.S., Macambira, M.J.B., 2009. The Mesoproterozoic Mucaja Mucajaí anorthosite–mangerite–rapakivi granite complex, Amazonian craton, Brazil. Canadian Mineralogist 47, 1469–1492.

Frost, B.R., Barnes, C.G., Collins, W.J., Arculus, R.J., Ellis, D.J., Frost, C.D., 2001. A geochemical classification for granitic rocks. J. Petrol. 41, 2033–2048.

Frost, B.R., Frost, C.D., 2008. A geochemical classification for feldspathic igneous rocks. J. Petrol. 49, 1955–1969.

Frost, C.D., Frost, B.R., 2011. On ferroan (A-type) granitoids: their compositional variability and modes of origin. J. Petrol. 52, 39–53.

Frost, C.D., Frost, B.R., 1997. Reduced rapakivi-type granites: the tholeiite connection. Geology 25, 647–650.

Frost, C.D., Frost, B.R., 2013. Proterozoic ferroan feldspathic magmatism. Precambr. Res. 228, 151–163.

Gehrels, G., Rusmore, M., Woodsworth, G., Crawford, M., Andronicos, C., Hollister, L., Patchett, J., Ducea, M., Butler, R., Klepeis, K., Davidson, C., Friedman, R., Haggart, J., Mahoney, B., Crawford, W., Pearson, D., Girardi, J., 2009. U-Th-Pb geochronology of the Coast Mountains batholith in north-coastal British Columbia: constraints on age and tectonic evolution. Geol. Soc. Am. Bull. 121, 1341–1361.

Gerdes, A., Zeh, A., 2006. Combined U-Pb and Hf isotope LA-(MC-)ICP-MS analyses of detrital zircons: comparison with SHRIMP and new constraints for the provenance and age of an Armorican metasediment in Central Germany. Earth Planet. Sci. Lett. 249, 47–61.

Gleißner, P., Drüppel, K., Taubald, H., 2010. Petrogenesis of anorthosites of the Mesoproterozoic Kunene Intrusive Complex, NW Namibia: evidence from stable and radiogenic isotope and lithophile and highly siderophile trace element composition. J. Petrol. 51, 897–919.

Gleißner, P., Drüppel, K., Romer, R.L., 2011. The role of crustal contamination in massif-type anorthosites, new evidence from Sr-Nd-Pb isotopic composition of the Kunene Intrusive Complex, NW Namibia. Precambr. Res. 185, 18–36.

Gleißner, P., Drüppel, K., Becker, H., 2012. Osmium isotopes and highly siderophile element fractionation in the massif-type anorthosites of the Mesoproterozoic Kunene Intrusive Complex, NW Namibia. Chem. Geol. 302–303, 33–47.

Gonçalves, L., Alkmim, F.F:, Pedrosa-Soares, A., Gonçalves, C.C:, Vieira, V., 2018. From the plutonic root to the volcanic roof of a continental magmatic arc: a review of the Neoproterozoic Araçuaí orogen, southeastern Brazil. International Journal of Earth Sciences 107, 337-358.

Goodge, J.W., Vervoort, J.D., 2006. Origin of Mesoproterozoic A-type granites in Laurentia: Hf isotope evidence. Earth Planet. Sci. Lett. 243, 711–731.

Hastie, A.R., Kerr, A.C., McDonald, I., Mitchell, S.F., Pearce, J.A., Millar, I.L., Barfod, D., Mark, D.F., 2010. Geochronology, geochemistry and petrogenesis of rhyodacite lavas in eastern Jamaica: a new adakite subgroup analogous to early Archaean continental crust? Chem. Geol. 276, 344–359.

Hayes, B., Lehmann, J., Bybee, G.M., Owen-Smith, T.M., 2022. Crystal transfer from magma to wallrock during syntectonic granite emplacement. jgs2020-125 J. Geol. Soc. 179 (1). https://doi.org/10.1144/jgs2020-125.

Heinonen, A.P., Andersen, T., Rämö, O.T., 2010. Re-evaluation of rapakivi petrogenesis: source constraints from the Hf Isotope Composition of Zircon in the rapakivi granites and associated mafic rocks of Southern Finland. J. Petrol. 51, 1687–1709.

Heinonen, A.P., Fraga, L.M., Rämö, O.T., Dall'Agnol, R., Mänttäri, I., Andersen, T., 2012. Petrogenesis of the igneous Mucajaí AMG complex, northern Amazonian craton – Geochemical, U-Pb geochronological, and Nd-Hf-O isotopic constraints. Lithos 151, 17-34.

Hoal, K.O., Hoal, B.G., Griffin, W.L., Armstrong, R.A., 2000. Characterization of the age and nature of the lithosphere in the Tsumkwe region, Namibia. In: Miller, R.McG. (Ed.), Special Issue: Henno Martin Commemorative Volume. Communications Geol. Survey Namibia 12, 21–28.

Irber, W., 1999. The lanthanide tetrad effect and its correlation with K/Rb, Eu/Eu*, Sr/Eu, Y/Ho, and Zr/Hf of evolving peraluminous granite suites. Geochim. Cosmochim. Acta 63, 489–508.

Irvine, T.N., Baragar, W.R.A., 1971. A guide to the chemical classification of the common volcanic rocks. Can. J. Earth Sci. 8, 523–548.

Jahn, B.-M., Wu, F., Capdevila, R., Martineau, F., Zhao, Z., Wang, Y., 2001. Highly evolved juvenile granites with tetrad REE patterns: the Wuduhe and Baderzhe granites from the Great Xing'an Mountains in NE China. Lithos 59, 171–198.

Jelsma, H.A., McCourt, S., Perritt, S.H., Armstrong, R.A., 2018. The geology and evolution of the Angolan Shield, Congo Craton. In: Siegesmund, S., Basei, M.A.S., Oyhantçabal, P., Oriolo, S. (Eds.), Geology of Southwest Gondwana. Springer International Publishing, Cham, pp. 217–239.

Jiang, X.Y., Luo, J.C., Guo, J., Wu, K., Zhang, Z.k., Sun, W.D., Xia, X.P., 2018. Geochemistry of I- and A-type granites of the Qingyang–Jiuhuashan complex, eastern China: Insights into Early Cretaceous multistage magmatism. Lithos 316–317, 278–294.

Koegelenberg, C., Kisters, A.F.M., Kramers, J.D., Frei, D., 2015. U-Pb detrital zircon and 39Ar–40Ar muscovite ages from the eastern parts of the Karagwe-Ankole Belt: tracking Paleoproterozoic basin formation and Mesoproterozoic crustal amalgamation along the western margin of the Tanzania Craton. Precambr. Res. 269, 147–161.

Konopásek, J., Cavalcante, C., Fossen, H., Janoušek, V., 2020. Adamastor – an ocean that never existed? Earth Sci. Rev. 103201 https://doi.org/10.1016/j.earscirev.2020.103201.

Kröner, A., Rojas-Agramonte, Y., 2017. Mesoproterozoic (Grenville-age) granitoids and supracrustal rocks in Kaokoland, northwestern Namibia. Precambr. Res. 298, 572–592.

Kröner, A., Rojas-Agramonte, Y., Hegner, E., Hoffmann, K.-H., Wingate, M.T.D., 2010. SHRIMP zircon dating and Nd isotopic systematics of Palaeoproterozoic migmatitic orthogneisses in the Epupa Metamorphic Complex of northwestern Namibia. Precambrian Research 183 (1), 50–69.

Kröner, A., Rojas-Agramonte, Y., Wong, J., Wilde, S.A., 2015. Zircon reconnaissance dating of Proterozoic gneisses along the Kunene River of northwestern Namibia. Tectonophysics 662, 125–139.

Langa, W.M., 2019. The petrology and economic potential of mafic-ultramafic intrusions west of the Kunene Anorthosite Complex, SW Angola, MSc thesis, university of Johannesburg, 114 pp.

Lee, Y., Cho, M., Yi, K., 2017. In situ U-Pb and Lu-Hf isotopic studies of zircons from the Sancheong-Hadong AMCG suite, Yeongnam Massif, Korea: Implications for the petrogenesis of ~1.86 Ga massif- type anorthosite. J. Asian Earth Sci. 138, 629–646.

Lee, S.-G., Masuda, A., Kim, H.S., 1994. An early Proterozoic leucogranitic gneiss with the REE tetrad phenomenon. Chem. Geol. 114, 59–67.

Lehmann, J., Bybee, G.M., Hayes, B., Owen-Smith, T.M., Belyanin, G., 2020. Emplacement of the giant Kunene AMCG complex into a contractional ductile shear zone and implications for the Mesoproterozoic tectonic evolution of SW Angola. Int. J. Earth Sci. https://doi.org/10.1007/s00531-020-01837-5.

Lenharo, S.L.R., Moura, M.A., Botelho, N.F., 2002. Petrogenetic and mineralization processes in Paleo- to Mesoproterozoic rapakivi granites: examples from Pitinga and Goiás, Brazil. Precambr. Res. 119, 277–299.

Littmann, S., Romer, R.L., Okrusch, M., 2000. Nephelinsyenite der Epembe-Swartbooisdrif-Alkali-Provinz (ESAP)/NW Namibia. Berichte der deutschen Mineralogischen Gesellschaft. Beih. Zum Eur. J. Mineral. 12, 115.

Loiselle, M.C., Wones, D.R., 1979. Characteristics and origin of anorogenic granites. Geol. Soc. Am. Abstracts with Programs 11 (3), 468.

Longhi, J., Ashwal, L.D., 1985. Two-stage models for lunar and terrestrial anorthosites: Petrogenesis without a magma ocean. Proceedings of the 15th Lunar and Planetary Science Conference, Part 2. Journal of Geophysical Research 90, C571–C584.

Longhi, J., Vander Auwera, J., Fram, M.S., Duchesne, J.-C., 1999. Some phase equilibrium constraints on the origin of Proterozoic (massif) anorthosites and related rocks. J. Petrol. 40, 339–362.

Ludwig, K., 2003. Isoplot/Ex version 3: A geochronological Toolkit for Microsoft Excel. Geochronology Center, Berkeley.

Lundmark, A.M., Corfu, F., 2008. Late-orogenic Sveconorwegian massif anorthosite in the Jotun Nappe Complex, SW Norway, and causes of repeated AMCG magmatism along the Baltoscandian margin. Contrib. Miner. Petrol. 155, 147–163.

Maier, W.D., Rasmussen, B., Fletcher, I.R., Li, C., Barnes, S.J., Huhma, H., 2013. The Kunene anorthosite complex, Namibia, and its satellite intrusions: geochemistry, geochronology, and economic potential. Econ. Geol. 108 (5), 953–986.

Mäkitie, H., Data, G., Isabirye, E., Mäntärri, I., Huhma, H., Klausen, M.B., Pakkenen, L., Virransaio, P., 2014. Petrology, geochronology and emplacement model of the giant 1.37 Ga arcuate Lake Victoria dyke swarm on the margin of a large igneous province in eastern Africa. J. Afr. Earth Sc. 97, 273–296.

Maniar, P.D., Piccoli, P.M., 1989. Tectonic discrimination of granitoids. Geol. Soc. Am. Bulletin 101, 635–643.

Masuda, A., Kawakami, O., Dohmoto, Y., Takenaka, T., 1987. Lanthanide tetrad effects in nature: two mutually opposite types, W and M. Geochem. J. 21, 119–124.

Mayer, A., Hofmann, A.W., Sinigoi, S., Morais, E., 2004. Mesoproterozoic Sm-Nd and U-Pb ages for the Kunene anorthosite complex of SW Angola. Precambr. Res. 133, 187–206.

McCourt, S., Armstrong, R.A., Jelsma, H., Mapeo, R.B.M., 2013. New U-Pb SHRIMP ages from the Lubango region, SW Angola: insights into the Palaeoproterozoic evolution of the Angolan Shield, southern Congo Craton, Africa. J. Geol. Soc. London 170 (2), 353–363.

McLelland, J.M., Bickford, M.E., Hill, B.M., Clechenko, C.C., Valley, J.W., Hamilton, M.A., 2004. Direct dating of Adirondack massif anorthosite by U-Pb SHRIMP analysis of igneous zircon: implications for AMCG complexes. Geol. Soc. Am. Bulletin 116, 1299–1317.

McLelland., J.M., Selleck, B.W., Hamilton, M.A., Bickford, M.E., 2010. Late- to post-tectonic setting of some major Proterozoic anorthosite – mangerite – charnockite – granite (AMCG) suites. Canadian Mineralogist 48, 729-750.

Meert, J.G., 2012. What's in a name? the columbia (Paleopangaea/Nuna) supercontinent. Gondwana Res. 21, 987–993.

Menge, G.F.W., 1986. Sodalite–carbonatite deposits of Swartbooisdrif, South West Africa/ Namibia. In: Anhaeusser, C.R., Maske, S. (Eds.), Mineral Deposits of Southern Africa. Geological Society of South Africa, Johannesburg, pp. 2261–2268.

Michot, P., 1960. La géologie de la catazone: le problème des anorthosites, la palingenése basique et la tectonique catazonale dans le Rogaland méridionale (Norvège méridionale). Norges Geologiske Undersøkelse Bulletin 212, 1–54.

Middlemost, E., 1994. Towards a comprehensive classification of igneous rocks and magmas. Earth-Sci. Rev. 31, 207–218.

Milani, L., Lehmann, J., Naydenov, K.V., Kinnaird, J.A., Saalmann, K., Daly, S., Frei, D., Lobo-Guerrero, S.A., 2015. A-type magmatism in a syn-collisional setting: the case of the Pan-African Hook Batholith in Central Zambia. Lithos 216, 48–72.

Miller, R.McG. 2008. The Geology of Namibia, volume 1 – Archaean to Mesoproterozoic. Geological Survey of Namibia, Windhoek. Ministry of Mines and Energy, Geological Survey, Windhoek, 309 pp.

Monecke, T., Kempe, U., Monecke, J., Sala, M., Wolf, D., 2002. Tetrad effect in rare earth element distribution patterns: a method of quantification with application to rock and mineral samples from granite-related rare metal deposits. Geochim. Cosmochim. Acta 66, 1185–1196.

Morais, E., Sinigoi, S., Mayer, A., Mucana, A., Miguel, L.G., Neto, J., 1998. The Kunene gabbro-anorthosite complex: preliminary results based on our new field and chemical data. African Geosci. Rev. 5 (4), 485–498.

Morse, S.A., 1982. A partisan review of Proterozoic anorthosites. Am. Mineral. 67, 1087–1100.

Moyen, J.F., Janoušek, V., Laurent, O., Bachmann, O., Jacob, J.B., Farina, F., Fiannacca, P., Villaros, A., 2021. Crustal melting vs. fractionation of basaltic magmas: Part 1, granites and paradigms. Lithos 106291.

Myers, J.S., Voordouw, R.J., Tettelaar, T.A., 2008. Proterozoic anorthosite– granite Nain batholith: structure and intrusion processes in an active lithosphere-scale fault zone, northern Labrador. Can. J. Earth Sci. 45, 909–934.

Nagaraju, J., Chetty, T.R.K., Prasad, G.S.V., Patil, S.K., 2008. Transpressional tectonics during the emplacement of Pasupugallu Gabbro Pluton, western margin of Eastern Ghats Mobile Belt, India: evidence from AMS fabrics. Precambr. Res. 162, 86–101.

Nakada, R., Shibula, T., Suzuki, K., Takahashi, Y., 2017. Europium anomaly variation under low-temperature water-rock interaction: a new thermometer. Geochem. Int. 55 (9), 822–832.

Pearce, J.A., 1996. Sources and settings of granitic rocks. Episodes 19, 120–125.

Pearce, J.A., Harris, N.B.W., Tindle, A.G., 1984. Trace element discrimination diagrams for the tectonic interpretation of granitic rocks. J. Petrol. 25, 956–983.

Pereira, E., Tassinari, C.G., Rodrigues, J.F., Van-Dúnen, M.V., 2011. New data on the deposition age of the volcano-sedimentary Chela Group and its Eburnean basement: implications to post-Eburnean crustal evolution of the SW of Angola. Comunicações Geológicas do LNEG 9, 27–40.

Rainaud, C., Master, S., Armstrong, R.A., Phillips, D., Robb, L.J., 2005. Monazite U-Pb dating and 40Ar/39Ar thermochronology of metamorphic events during the Lufilian orogeny, Central African Copperbelt. J. Afr. Earth Sc. 42 (1–5), 183–199.

Rämö, O.T., Haapala, I., 2005. Rapakivi granites. In: Lehtinen, M., Nurmi, P.A., Rämö, O. T. (Eds.), Precambrian Geology of Finland Key to the Evolution of the Fennoscandian Shield, vol. 14. Developments in Precambrian Geology, 533–562.

Ren, L., Liang, H., Bao, Z., Huang, W., 2021. Oblique continental collision and the formation of syn-collisional A-type granites: insights from the Early Jurassic Baoji granite suite in the Qinling orogenic belt, central China. Int. Geol. Rev. 1–22.

Rivers, T., 2008. Late Mesoproterozoic to Early Neoproterozoic (Geons 11–10) magmatism on SE Laurentia – implications for the tectonic setting of AMCG complexes. Geol. Assoc. Can. - Mineral. Assoc. Can., Program Abstracts 33, 144.

Rivers, T., Corrigan, D., 2000. Convergent margin on southeastern Laurentia during the Mesoproterozoic: tectonic implications. Can. J. Earth Sci. 37, 359–383.

Romick, J.D., Kay, S.M., Kay, R.W., 1992. The influence of amphibole fractionation on the evolution of calc-alkaline andesite and dacite tephra from the central Aleutians, Alaska. Contrib. Miner. Petrol. 112, 101–118.

Rudnick, R.L., Gao, S., 2003. Composition of the continental crust. In: Rudnick, R.L. (Ed.), The Crust. Elsevier-Pergamon, Oxford, UK, pp. 1–64.

Scoates, J.S., 2000. The plagioclase–magma density paradox re-examined and the crystallization of Proterozoic anorthosites. J. Petrol. 41, 627–649.

Scoates, J.S., Chamberlain, K.R., 1997. Orogenic to post-orogenic origin for the 1.76 Ga Horse Creek Anorthosite Complex, Wyoming, USA. J. Geol. 105, 331–344.

Scoates, J.S., Chamberlain, K.R., 2003. Geochronologic, geochemical and isotopic constraints on the origin of monzonitic and related rocks in the Laramie anorthosite complex, Wyoming, USA. Precambr. Res. 124, 269–304.

Seth, B., Armstrong, R.A., Brandt, S., Villa, I.M., Kramers, J.D., 2003. Mesoproterozoic UPb and Pb–Pb ages of granulites in NW Namibia: reconstructing a complete orogenic cycle. Precambr. Res. 126 (1–2), 147–168.

Seth, B., Armstrong, R.A., Büttner, A., Villa, I.M., 2005. Time constraints for Mesoproterozoic upper amphibolite facies metamorphism in NW Namibia: a multi-isotopic approach. Earth Planet. Sci. Lett. 230 (3–4), 355–378.

Seth, B., Kröner, A., Mezger, K., Nemchin, A.A., Pidgeon, R.T., Okrusch, M., 1999. Archaean to Neoproterozoic magmatic events in the Kaoko belt of NW Namibia and their geodynamic significance. Precambr. Res. 92, 341–363.

Shumlyanskyy, L., Billström, K., Hawkesworth, C., Elming, S.Å., 2012. U-Pb age and Hf isotope compositions of zircons from the north-western region of the Ukrainian shield: mantle melting in response to post-collision extension. Terra Nova 24, 373–379.

Shumlyanskyy, L., Hawkesworth, C., Billström, K., Bogdanova, S., Mytrokhyn, O., Romer, R., Dhuime, B., Claesson, S., Ernst, R., Whitehouse, M., Bilan, O., 2017. The origin of the Palaeoproterozoic AMCG complexes in the Ukrainian shield: New U-Pb ages and Hf isotopes in zircon. Precambr. Res. 292, 216–239.

Singletary, S.J., Hanson, R.E., Martin, M.W., Crowley, J.L., Bowring, S.A., Key, R.M., Ramokate, L.V., Direng, B.B., Krol, M.A., 2003. Geochronology of basement rocks in the Kalahari Desert, Botswana, and implications for regional Proterozoic tectonics. Precambr. Res. 121, 47–71.

Slagstad, T., Roberts, N.M.W., Coint, N., Høy, I., Sauer, S., Kirkland, C.L., Marker, M., Røhr, T.S., Henderson, I.H.C., Stormoen, M.A., Skår, Ø., Sørensen, B.E., Bybee, G.M., 2018. Magma-driven, high-grade metamorphism in the Sveconorwegian Province, southwest Norway, during the terminal stages of Fennoscandian Shield evolution. Geosphere 14 (2), 861–882.

Slagstad, T., Henderson, I.H.C., Roberts, N.M.W., Kulakov, E.V., Ganerød, M., Kirkland, C.L., Dalslåen, B., Creaser, R.A., Coint, N., 2022. Anorthosite formation and emplacement coupled with differential tectonic exhumation of ultrahigh-temperature rocks in a Sveconorwegian continental back-arc setting. Precambr. Res. 376, 106695.

Slejko, F.F., Demarchi, G., Morais, E., 2002. Mineral chemistry and Nd isotopic composition of two anorthositic rocks from the Kunene complex (South Western Angola). J. Afr. Earth Sc. 35, 77–88.

Stern, C.R., 2011. Subduction erosion: Rates, mechanisms, and its role in arc magmatism and the evolution of the continental crust and mantle. Gondwana Res. 20, 284–308.

Tack, L., Williams, I., Bowden, P., 2002. SHRIMP constraints on early post-collisional granitoids of the Ida Dome, Central Damara (Pan- African) Belt, western Namibia. In: Extended Abstracts, 11th Quadrennial IAGOD Symposium and Geocongress 2002, 22–26 July 2002, Windhoek, Namibia.

Tack, L., Wingate, M.T.D., De Waele, B., Meert, J., Belousova, E., Griffin, B., Tahon, A., Fernandez-Alonso, M., 2010. The 1375 Ma "Kibaran event" in central Africa: prominent emplacement of bimodal magmatism under extensional regime. Precambr. Res. 180, 63–84.

Tang, M., Wang, X.-L., Shu, X.-J., Wang, D., Yang, T., Gopon, P., 2014. Hafnium isotopic heterogeneity in zircons from granitic rocks: Geochemical evaluation and modelling of "zircon effect" in crustal anatexis. Earth Planet. Sci. Lett. 389, 188–199.

Torquato, J.R., Ferreira da Silva, A.T., Cordani, U.G., Kawashita, K., 1979. Evolução Geológica do Cinturão Móvel do Quipungo no Ocidente de Angola. Anais da Academia Brasileira de Ciências 51, 133–143.

Vander Auwera, J., Bolle, O., Bingen, B., Liégeois, J.-P., Bogaerts, M., Duchesne, J.C., De Waele, B., Longhi, J., 2011. Sveconorwegian massif-type anorthosites and related granitoids result from post-collisional melting of a continental arc root. Earth-Sci. Rev. 107, 375–397.

Vauchez, A., Hollanda, M.H.M.Z., Monié, P., Mondou, M., Egydio-Silva, M., 2019. Slow cooling and crystallization of the roots of the Neoproterozoic Araçuaí hot orogen (SE Brazil): implications for rheology, strain distribution, and deformation analysis. Tectonophysics 766, 500–518. https://doi.org/10.1016/j.tecto.2019.05.013.

Villaros, A., Buick, I.S., Stevens, G., 2012. Isotopic variations in S-type granites: an inheritance from a heterogeneous source? Contribution to Mineral. Petrol. 163, 243–257.

Wang, Y., Yang, Y.-Z., Siebel, W., Zhang, H., Zhang, Y.-S., Chen, F., 2020. Geochemistry and tectonic significance of late Paleoproterozoic A-type granites along the southern margin of the North China Craton. Nat. Scientific Reports 10 (1), 1–15.

Whalen, J.B., Currie, K.L., Chappell, B.W., 1987. A-type granites: geochemical characteristics, discrimination and petrogenesis. Contribution to Mineral. Petrol. 95, 407–419.

Whattam, S.A., Stern, R.J., 2015. Arc magmatic evolution and the construction of continental crust at the Central American Volcanic Arc system. Int. Geol. Rev. 58 (6), 653–686.

Wiebe, R.A., 1992. Proterozoic anorthosite complexes. In: Condie, K.C. (Ed.), Proterozoic crustal evolution: New York. Elsevier, NY, pp. 215–261.

Wood, D.A., Joron, J.L., Treuil, M., Norry, M., Tarney, J., 1979. Elemental and Sr isotope variations in basic lavas from Iceland and the surroundings ocean floor. Contrib. Miner. Petrol. 70, 319–339.

Wu, F.-Y., Sun, D.-Y., Li, H., Jahn, B.-M., Wilde, S., 2002. A-type granites in northeastern China: age and geochemical constraints on their petrogenesis. Chem. Geol. 187, 143–173.

Zeng, L.-S., Saleeby, J.B., Asimow, P., 2005. Nd isotopic disequilibrium during crustal anatexis: a record from the Goat Ranch migmatite complex, southern Sierra Nevada batholith. California Geology 33, 53–56.

Zhao, K.-D., Jiang, S.-Y., Chen, W.-F., Chen, P.-R., Ling, H.-F., 2013. Zircon U-Pb chronology and elemental and Sr–Nd–Hf isotope geochemistry of two Triassic A-type granites in South China: implication for petrogenesis and Indosinian transtensional tectonism. Lithos 160, 292–306.

Zhao, T.-P., Chen, W., Zhou, M.-F., 2009. Geochemical and Nd-Hf isotopic constraints on the origin of the ~1.74 Ga Damiao anorthosite complex. North China Craton. Lithos 113, 673–690.